

Synthetic Spectral Library of Optically Thick Atmospheres for Little Red Dots

HANPU LIU (刘翰溥) ¹, YAN-FEI JIANG (姜燕飞) ², ELIOT QUATAERT ¹, JENNY E. GREENE ¹,
YILUN MA (马逸伦) ¹ AND XIAOJING LIN ³

¹*Department of Astrophysical Sciences, Princeton University, 4 Ivy Lane, Princeton, NJ 08544, USA*

²*Center for Computational Astrophysics, Flatiron Institute, New York, NY 10010, USA*

³*Department of Astronomy, Tsinghua University, Beijing 100084, China*

ABSTRACT

Little Red Dots (LRDs) challenge conventional models of active galactic nuclei. At rest-optical-to-near-infrared (IR) wavelengths, these compact extragalactic objects show blackbody-like continuum emission and spectral features reminiscent of stars, motivating models with an optically thick atmosphere at $T_{\text{eff}} \sim 4000 - 5000$ K. We develop (and publicly release) a synthetic spectral library of optically thick atmospheres with gas conditions tailored for LRDs, parameterized by effective temperature T_{eff} and surface gravity g . Given the uncertain dynamical structure of LRDs, we interpret g most directly as a photospheric density ρ_{ph} . We show that blackbodies are only crude approximations to the emission from LRD-like atmospheres. Spectral features are abundant, many of which are sensitive diagnostics of photospheric density, including the overall curvature of the spectral energy distribution, the rest-1.6 μm spectral “kink” from H^- opacity, and the Ca II triplet (CaT) absorption at rest-8500 \AA . When compared against a local LRD, *the Egg*, all three features consistently indicate a low photospheric density of $\rho_{\text{ph}} \sim 10^{-11} \text{ g cm}^{-3}$ ($g \sim 10^{-3} \text{ cm s}^{-2}$ in our library). This disfavors hydrostatic configurations and suggests a mass within the photosphere (black hole plus gas) of $10^4 M_{\odot}$, with an Eddington ratio $\lambda_{\text{Edd}} \gtrsim 20$, if the CaT width traces turbulent support at the photosphere in spherical symmetry; the inferred mass could be higher depending on the geometry and the radius probed by CaT. For higher redshift LRDs, we advocate for rest-near-IR spectroscopic surveys and high-resolution spectra of potential absorption lines as a test of the optically thick atmosphere scenario and as a unique probe of the central engine mass.

Keywords: Active galactic nuclei (16), Radiative transfer (1335), Accretion (14)

1. INTRODUCTION

The so-called “Little Red Dots” (LRDs, I. Labbé et al. 2023; D. D. Kocevski et al. 2023; J. Matthee et al. 2024) remain a mystery in extragalactic astronomy. Their broad, luminous emission lines likely indicate a supermassive black hole as the central engine, yet other features set them apart from any previously known population of active galactic nuclei (AGN). Their spectral energy distribution (SED) shows a red rest-optical color and a turnover in the near-infrared (near-IR), resembling a blackbody at $T_{\text{eff}} \sim 5000$ K (e.g., A. de Graaff et al. 2025a; H. Umeda et al. 2025; K. Inayoshi & L. C. Ho 2025). This blue near-IR color, combined with non-detections in the rest-mid-to-far-IR, stringently limits the amount of dust attenuation (C. C. Williams et al.

2024; H. B. Akins et al. 2024; D. J. Setton et al. 2025; M. Xiao et al. 2025; C. M. Casey et al. 2025; K. Chen et al. 2025), leaving the red rest-optical unexplained by conventional AGN-galaxy composite models (J. F. W. Baggen et al. 2024; I. Labbe et al. 2024; B. Wang et al. 2025; Y. Ma et al. 2025). Furthermore, LRDs do not show the strong X-ray or short-term variability expected from accretion near a black hole (M. Yue et al. 2024; T. T. Ananna et al. 2024; R. Maiolino et al. 2025; A. Sacchi & A. Bogdan 2025; M. Kokubo & Y. Harikane 2024; Z. Zhang et al. 2025a; C. J. Burke et al. 2025), which further suggests a physical nature different from typical AGN.

A family of models have invoked spherically symmetric, optically thick atmospheres to explain the observational puzzles (“black hole star”, R. P. Naidu et al. 2025; gas envelope, D. Kido et al. 2025; spherical super-Eddington accretion, H. Liu et al. 2025; late-stage

“quasi-star”, M. C. Begelman & J. Dexter 2025; A. D. Santarelli et al. 2025; supermassive star, D. Nandal & A. Loeb 2026). The photosphere of the gas naturally produces blackbody-like emission at $T_{\text{eff}} \sim 5000$ K due to the steep temperature dependence of the hydrogen opacity, which shares a physical origin with the Hayashi track in stellar evolution (C. Hayashi 1961). The optically thick gas will suppress any X-rays formed near the black hole. The large photosphere radius implies no variability below a timescale measured in decades (Z. Zhang et al. 2025b). This scenario, if further confirmed, will redefine our current understanding of accretion physics and black hole evolution.

To test these models against the rich spectral data, one needs model predictions more detailed than a blackbody. The SEDs of stars are known to deviate from a blackbody, and so do those of LRDs (A. de Graaff et al. 2025a). It remains unclear under what conditions optically thick gas can reproduce the observed SED shape and various spectral features of LRDs. Some works have used existing stellar spectral libraries to compare to observed LRDs or make model predictions (e.g., A. de Graaff et al. 2025b; X. Ji et al. 2025a; A. D. Santarelli et al. 2025; B. Wang et al. 2026), but, as noted in H. Liu et al. (2025) and A. D. Santarelli et al. (2025) from different perspectives, the LRD atmosphere may have densities below those of stars. The emission properties of such low-density atmospheres need modeling to connect theory with observation.

On the observational side, inferences of the black hole mass based on the broad Balmer emission lines are uncertain by orders of magnitude, with ongoing debates over the broadening mechanism of these lines (A. King 2024; V. Rusakov et al. 2026; R. P. Naidu et al. 2025; S.-J. Chang et al. 2026; A. Torralba et al. 2025; A. Sneppen et al. 2026; I. Judžbalis et al. 2024; M. Brazzini et al. 2025, 2026). Independent constraints on the black hole mass are in high demand. A different methodology is widely adopted in the stellar community: spectral features that originate from the photosphere, e.g., absorption lines, are sensitive tracers of the atmosphere conditions, and fitting theoretical spectra to data constrains parameters such as the effective temperature, surface gravity, and metallicity. As the SED of LRDs resembles stars in the rest-optical to near-IR, a similar approach, i.e., calculating model atmospheres and synthetic spectra from first principles and then comparing them to observations, may provide unique insights to the photosphere properties of LRDs and thus reveal information about their central engines.

In this work, we construct one-dimensional model atmospheres with radiative transfer and use them to in-

terpret the optical-to-near-IR portion of the LRD spectra. Our approach is analogous to established stellar synthetic spectral libraries (e.g., R. L. Kurucz 1979; B. Gustafsson et al. 2008; P. H. Hauschildt et al. 2025), but we focus on relatively low gas densities (typically $10^{-12} - 10^{-8}$ g cm $^{-3}$ at the photosphere) and effective temperatures around 5000 K, a parameter space tailored for LRDs but not fully covered in existing libraries. Our synthetic spectra provide a direct testing ground for optically thick envelope models of LRDs and suggest continuum- and absorption line-based observational diagnostics of their physical properties. Our spectral library is publicly available on GitHub⁴; we welcome requests to add calculations for parameters not yet included.

This paper is organized as follows. In Section 2, we outline our methods and interpretation of the model parameters. Section 3 describes our model grid. Section 4 elaborates on the continuum and line features as potential diagnostics for LRDs. In Section 5, we apply our library to a local LRD and argue for its likely low mass of the central engine. We summarize our work and discuss caveats, implications for modeling, and prospects for observation in Section 6. Throughout this work, we refer to radiation frequencies and wavelengths in the rest frame unless otherwise noted. We adopt the Planck Collaboration et al. (2016) cosmological parameters, i.e., $\Omega_m = 0.307$, $\Omega_\Lambda = 0.693$, $\Omega_b = 0.0486$, and $H_0 = 67.7$ km s $^{-1}$ Mpc $^{-1}$, and use the AB magnitude system.

2. METHODS

We use TLUSTY (Version 208, I. Hubeny 1988; I. Hubeny et al. 2021) to construct atmosphere models for LRDs. The open-source code has been widely used for both stellar (e.g., T. Lanz & I. Hubeny 2007; Y. Osorio et al. 2020) and AGN accretion disk (e.g., I. Hubeny & V. Hubeny 1998; I. Hubeny et al. 2001; Y. Hui et al. 2005) spectral modeling. The physics and numerical algorithms have been detailed in I. Hubeny & T. Lanz (2017); here, we summarize its key features relevant to this work and describe our setup.

The stellar mode of TLUSTY evaluates one-dimensional radiative and hydrostatic equilibrium equations and produces an atmosphere model parameterized by the effective temperature T_{eff} and surface gravity g . The code assumes plane-parallel geometry. The validity of this approximation for LRDs is uncertain but plausible, given their large photosphere radii compared to the atmosphere scale height in most of our

⁴ https://github.com/hanpu-liu/LRD_synthetic_spectral_library

models, as we shall see in Section 2.1; we will further discuss the gas geometry in Section 5.2. We assume local thermal equilibrium (LTE), i.e., the ionization stage and level population of all species follow a thermal distribution, fully described by the local gas temperature and density; we will briefly discuss non-LTE effects in Section 6.1. We parameterize the gas metallicity $[M/H]$ scaled from the solar abundance in M. Asplund et al. (2009). We set a default microturbulence velocity of $\xi_{\text{mtb}} = 2 \text{ km s}^{-1}$ but also include $\xi_{\text{mtb}} = 10 \text{ km s}^{-1}$ for a subset of our models. We set a convection mixing length of 1.25 for all of our models.

Solving the radiative transfer equation requires knowing the frequency-dependent opacity at each location in the atmosphere. We use the opacity table functionality in SYNSPEC (Version 54, I. Hubeny 1988; I. Hubeny et al. 2021), the companion code to TLUSTY, to pre-compute the absorption opacity in the wavelength range of $900 \text{ \AA} < \lambda < 110000 \text{ \AA}$ over 30000 logarithmically equidistant frequency points. We tested using 100000 frequency points and found negligible differences in the resulting atmospheres. We include the line lists of atoms, ions, 19 diatomic molecules (H_2 , C_2 , CH , CN , CO , N_2 , NH , NO , O_2 , OH , MgH , MgC , MgN , MgO , SiH , SiC , SiN , SiO , and TiO), and water (H_2O). The atomic and diatomic molecular line lists (except for TiO) are based on Kurucz’s list (R. L. Kurucz 2019) and updated with data from the National Institute of Standards and Technology database whenever possible, while the TiO and H_2O line lists are taken from the ExoMol database (L. K. McKemmish et al. 2019; O. L. Polyansky et al. 2018) (with rejection parameters of -8.5 and -9 respectively); more detailed descriptions can be found in I. Hubeny et al. (2021), and the full line lists are available in the TLUSTY software package indicated in that paper. Molecules are considered both in opacity and in the equation of state.

The converged model atmosphere from TLUSTY is then passed to SYNSPEC for detailed spectral synthesis. For the Ca H and K resonance lines, we consider partial frequency redistribution (PFR), an effect that is particularly important for low-density atmospheres and strongly impacts the predicted line equivalent widths. We illustrate this point and describe our treatment in Appendix A. Where our parameter space overlaps with the stellar regime, we compare our spectra with two stellar synthetic spectral libraries, MARCS (B. Gustafsson et al. 2008) and NewEra (P. H. Hauschildt et al. 2025), and find good agreement; see Appendix B.

2.1. Interpretation of gravity

In this subsection, we elaborate on the treatment of hydrostatic equilibrium in our models and the corresponding interpretation of the parameter g . This is the parameter of highest interest in this work since it is related to the central mass (see below). We emphasize that radiative transfer, which gives rise to spectral features, does not directly know about gravity. The parameter g only indirectly influences the predicted spectrum by changing the photosphere density (see Equation (4) below) and thus the opacities and optical depths.

In general, at each atmosphere layer, the equation of motion in the radial direction is given by a balance between gravity, dynamical motion of the gas, and accelerations driven by gas pressure dP_{gas}/dm (where m is the column mass) and radiation g_{rad} :

$$g - g_{\text{dyn}} - \frac{dP_{\text{gas}}}{dm} = g_{\text{rad}} = \frac{\kappa_F \sigma T_{\text{eff}}^4}{c} = 0.40 \text{ cm s}^{-2} \kappa_{0.34} T_5^4, \quad (1)$$

where κ_F is the flux-mean opacity, $\kappa_{0.34} \equiv \kappa_F / (0.34 \text{ cm}^2 \text{ g}^{-1})$ ($\kappa_{0.34} = 1$ for the electron-scattering opacity of fully ionized gas), and $T_5 \equiv T_{\text{eff}} / (5000 \text{ K})$. Among these terms, g_{dyn} can be estimated by

$$g_{\text{dyn}} \simeq -\text{sgn} \left(\frac{dv^2}{dR} \right) \frac{v^2}{R}, \quad (2)$$

where v and R are the characteristic velocity and radius of the gas layer in question. We also define

$$g_{\text{net}} \equiv g - g_{\text{dyn}} \quad (3)$$

as a shorthand. If the gas is bound, including inflows, rotation, turbulence, or failed outflows, we expect $dv^2/dR < 0$ and thus $g_{\text{dyn}} > 0$, which tends to cancel gravity, i.e., $g_{\text{net}} < g$; in the limiting case of virial motion, $g_{\text{net}} \ll g$. For outflows that successfully escape the system, we expect $dv^2/dR > 0$ and thus $g_{\text{net}} > g$.

We note that g_{net} can also be understood as a way of parameterizing the photosphere gas density. Denoting the gas density, Rosseland-mean opacity, and scale height at the photosphere as ρ_{ph} , κ_{ph} , and H_{ph} , we have $\rho_{\text{ph}} \kappa_{\text{ph}} H_{\text{ph}} \sim 2/3$ and $dP_{\text{gas}}/dm \sim k_B T_{\text{eff}} / \mu m_p H_{\text{ph}}$, and thus

$$\rho_{\text{ph}} \sim \frac{2\mu m_p (g_{\text{net}} - g_{\text{rad}})}{3k_B T_{\text{eff}} \kappa_{\text{ph}}} = 2.1 \times 10^{-9} \text{ g cm}^{-3} \mu_{1.3} g_0 T_5^{-1} \kappa_{-3}^{-1}, \quad (4)$$

$$H_{\text{ph}} \sim \frac{k_B T_{\text{eff}}}{\mu m_p (g_{\text{net}} - g_{\text{rad}})} = 3.2 \times 10^{11} \text{ cm } \mu_{1.3}^{-1} g_0^{-1} T_5, \quad (5)$$

where μ is the mean molecular weight, m_p is the proton mass, $\mu_{1.3} \equiv \mu / 1.3$, $g_0 \equiv (g_{\text{net}} - g_{\text{rad}}) / (1 \text{ cm s}^{-2})$, and $\kappa_{-3} \equiv \kappa_{\text{ph}} / (10^{-3} \text{ cm}^2 \text{ g}^{-1})$. In the usual case that

κ_{ph} does not sharply decrease with ρ_{ph} , the photosphere gas density will increase with net gravity. We also note that the photosphere radius of LRDs can be estimated as $R_{\text{ph}} = \sqrt{L_{\text{atm}}/4\pi\sigma T_{\text{eff}}^4} = 1.5 \times 10^{16}$ cm for a total atmosphere luminosity $L_{\text{atm}} = 10^{44}$ erg s $^{-1}$ and $T_{\text{eff}} = 5000$ K. This is much greater than the photosphere scale height in Equation (5) unless $g_{\text{net}} - g_{\text{rad}} \lesssim 10^{-4}$ cm s $^{-2}$, which justifies the plane-parallel assumption. Finally, the surface gravity g is related to the total mass (including the black hole and gas) enclosed by the photosphere M_{tot} by

$$g = \frac{4\pi\sigma T_{\text{eff}}^4 GM_{\text{tot}}}{L_{\text{atm}}} = 0.60 \text{ cm s}^{-2} M_6 T_5^4 L_{44}^{-1}, \quad (6)$$

where $M_6 \equiv M_{\text{tot}}/(10^6 M_{\odot})$, and $L_{44} \equiv L_{\text{atm}}/(10^{44} \text{ erg s}^{-1})$.

In the calculations that follow, we neglect dynamical motion since it is not part of the hydrostatic calculations in TLUSTY. We reiterate, however, that radiative transfer is separate from dynamics (aside from Doppler shifts which can modify the opacities but are also not included in TLUSTY). For a given effective temperature and photosphere density, we expect models with dynamical motions to give similar spectral features and continuum emission as the hydrostatic models considered here. Since ρ_{ph} only depends on g_{net} rather than separately on g and g_{dyn} , we can constrain g_{net} using the spectral library while being agnostic about the dynamical environment (i.e., g and g_{dyn} can vary individually subject to the constraint of g_{net}). In this sense, our spectral library applies not only to quasi-star-like models but also at least semi-quantitatively to disk models (C. Zhang et al. 2025; L. Zwick et al. 2025; Y.-X. Chen et al. 2026) and quasi-spherical accretion (H. Liu et al. 2025) as long as the energy source is deep within the optically thick atmosphere. In what follows, we use “ g ” as a model parameter but interpret it as g_{net} . We can then recover the physical gravity and hence the atmosphere-scale total mass using independent constraints on g_{dyn} (e.g., from line broadening). We will show such analysis later in Section 5.

2.2. Treatment of super-Eddington scenarios

Low-gravity models potentially become super-Eddington, i.e., with $g < g_{\text{rad}}$ in some part of the atmosphere. Note that g_{rad} varies by orders of magnitude within a single atmosphere: at $3000 \text{ K} \lesssim T \lesssim 8000 \text{ K}$, the opacity sharply increases with temperature, so the inner, hotter layers of the atmosphere usually have higher g_{rad} and more easily become super-Eddington. This leads to two regimes:

A. When g is moderately low, the outer layers still satisfy $g > g_{\text{rad}}$ while the inner ones reach $g < g_{\text{rad}}$ and

thus $dP_{\text{gas}}/dm < 0$. This will give rise to a gas pressure maximum, $P_{\text{gas,max}}$, at $g = g_{\text{rad}}$. We modify the hydrostatic assumption by setting $P_{\text{gas}} = P_{\text{gas,max}}$ in the super-Eddington layers, with the rationale that gas pressure inversion is unstable and that the inner atmosphere may dynamically smear out this inversion layer (Y.-F. Jiang et al. 2015). This dynamical modification does not strongly influence the synthetic spectra as the outer layers, where most spectral features form, remain in hydrostatic equilibrium. In the rest of this work, we refer to models with hydrostatic upper layers as “hydrostatic” irrespective of whether they have super-Eddington inner layers.

B. For even lower g , the entire atmosphere becomes super-Eddington. We explore a few cases in this regime by removing radiation acceleration from the hydrostatic equation altogether. In this case, our physical interpretation is no longer an atmosphere model with a hydrostatic structure, but rather an optically thick gas layer with a prescribed (but dynamically unphysical) gas pressure structure given by $dP_{\text{gas}}/dm = g$. Equation (4) is still valid here, with $g_{\text{rad}} = 0$, and the low g_{net} allows us to obtain low ρ_{ph} . In reality, such low-density atmospheres are likely spatially extended with strong gas motion, e.g., in the form of a wind, where our code assumptions break down. The setup here aims only to illustrate the spectral properties of gas emitting at a very low density. In all figures in this work, we will use filled markers for hydrostatic model points and empty markers for models with g_{rad} turned off.

3. MODEL GRIDS

Figure 1 outlines the parameter space explored in this work in the dimensions of T_{eff} , $\log g$, and $[\text{M}/\text{H}]$. The model grid spans a range of $2000 \text{ K} \leq T_{\text{eff}} \leq 7500 \text{ K}$ and is densest at $T_{\text{eff}} = 4500 - 5000 \text{ K}$, motivated by LRDs clustering at this optical color temperature (A. de Graaff et al. 2025a). Our calculations mainly cover $[\text{M}/\text{H}] = -1$; we will show later that different metallicities significantly change metal absorption features but only mildly influence the spectral continuum. While Figure 1 only shows models with $\xi_{\text{mtb}} = 2 \text{ km s}^{-1}$, we also include $\xi_{\text{mtb}} = 10 \text{ km s}^{-1}$ for hydrostatic models with $4000 \text{ K} \leq T_{\text{eff}} \leq 5000 \text{ K}$ and $[\text{M}/\text{H}] = -1$; we will show later that microturbulence tends to redden the UV to blue-optical portion of the SED by metal line-blocking but has negligible impact on the continuum at longer wavelengths. As for the range of g , we reach a maximum of $\log g = 1.5$ (in cm s $^{-2}$), which corresponds to $M_{\text{tot}} \sim 10^8 M_{\odot}$ according to Equation (6) if assuming radial hydrostatic equilibrium. For each T_{eff} , we decrease $\log g$ until the upper atmosphere becomes

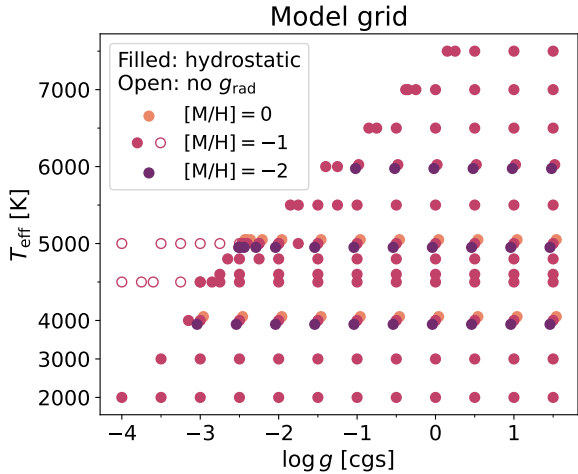


Figure 1. Grid of model parameters covered in this work. Points with multiple metallicity coverage are slightly shifted for visual clarity. The vertical plotting scale is different below 4000 K, where coverage is sparser. Only models with $\xi_{\text{mtb}} = 2 \text{ km s}^{-1}$ are shown, but we also calculated hydrostatic models with $\xi_{\text{mtb}} = 10 \text{ km s}^{-1}$, $4000 \text{ K} \leq T_{\text{eff}} \leq 5000 \text{ K}$, and $[\text{M}/\text{H}] = -1$. For the meaning of “hydrostatic” (filled markers) versus “no- g_{rad} ” (empty markers) models, see Section 2.2.

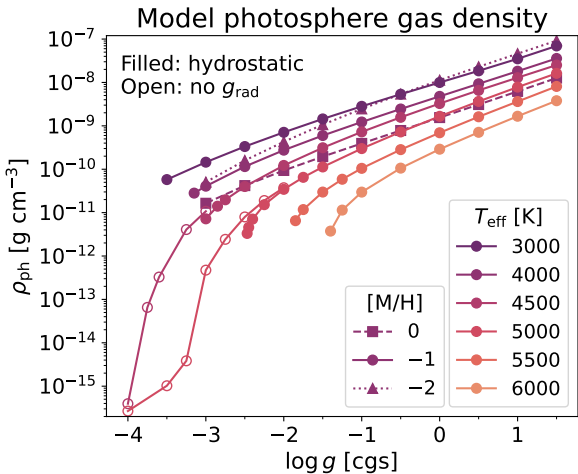


Figure 2. Photosphere gas density ρ_{ph} as a function of gravity. Multiple metallicities are shown only for $T_{\text{eff}} = 4000 \text{ K}$ for visual clarity. Only models with $\xi_{\text{mtb}} = 2 \text{ km s}^{-1}$ are shown; results are similar for $\xi_{\text{mtb}} = 10 \text{ km s}^{-1}$. For the meaning of “hydrostatic” (filled markers) versus “no- g_{rad} ” (empty markers) models, see Section 2.2. For a given T_{eff} and $[\text{M}/\text{H}]$, ρ_{ph} increases with $\log g$.

super-Eddington (Section 2.1) or until $\log g = -4$. This gives the left boundary of the filled circles in Figure 1. For $T_{\text{eff}} = 4500 \text{ K}$ and 5000 K , we further explore the scenario with g_{rad} turned off and reach $\log g = -4$.

The low end of the gravity range, which implies $M_{\text{tot}} \sim 10^3 M_{\odot}$ by Equation (6), seems implausible if

LRDs are in radial hydrostatic equilibrium. However, the photosphere densities that these $\log g$ values represent are possible in alternative scenarios. Figure 2 shows the photosphere gas density, ρ_{ph} , as a function of $\log g$. We measure ρ_{ph} from the converged model atmospheres at the location where the Rosseland-mean optical depth is equal to $2/3$. For a given T_{eff} and $[\text{M}/\text{H}]$, ρ_{ph} increases with $\log g$, as expected from Equation (4). For $T_{\text{eff}} = 5000 \text{ K}$, a factor of 10 higher or lower metallicity from the fiducial value of $[\text{M}/\text{H}] = -1$ introduces a change of ρ_{ph} by a factor < 3 ; the same is true for $T_{\text{eff}} = 4000 \text{ K}$ and 6000 K , although not shown in the figure. Microturbulence does not strongly influence the photosphere density, with ρ_{ph} differing by a factor < 1.5 between $\xi_{\text{mtb}} = 2 \text{ km s}^{-1}$ and 10 km s^{-1} . Most radially hydrostatic models have $\rho_{\text{ph}} \gtrsim 10^{-11} \text{ g cm}^{-3}$. However, the disk models in L. Zwick et al. (2025); Y.-X. Chen et al. (2026) and the super-Eddington accretion model in H. Liu et al. (2025) do reach densities of the order $10^{-12} \text{ g cm}^{-3}$ or lower even with high central masses. For these scenarios, Figure 2 is the tool to convert “ $\log g$ ” as a density parameter to the physically meaningful ρ_{ph} . We note that our grid reaches much lower $\log g$ than stellar synthetic spectral libraries, which typically cover $\log g \geq 0$.

In Figure 2, at $T_{\text{eff}} = 5000 \text{ K}$ and $[\text{M}/\text{H}] = -1$, the hydrostatic branch (where we account for g_{rad}) and the branch without g_{rad} agree at $\log g \gtrsim -2.25$ and only diverge below this. Meanwhile, we cannot find a hydrostatic solution at $\log g \leq -2.48$, indicating that, at the photosphere, $\log g_{\text{rad}} \approx -2.48$. This implies that radiation acceleration only strongly influences ρ_{ph} when g approaches g_{rad} at the photosphere, as expected from Equation (4). We note that $\log g_{\text{rad}} \approx -2.48$ is much lower than the radiative acceleration of the inner, fully ionized layers (Equation (1)) due to the much lower opacity at the photosphere.

4. SYNTHETIC SPECTRA

In this section, we investigate several continuum and line features of our synthetic spectra, in particular their parametric dependence and their observational utility in diagnosing the physical conditions of LRDs.

Figure 3 gives an overview of the synthetic spectra. We can qualitatively match the optical-to-near-IR spectra of LRDs such as UNCOVER-45924 (I. Labbe et al. 2024) or J1025+1402 (nicknamed *the Egg*, X. Lin et al. 2025) using a single T_{eff} , in agreement with the findings in A. de Graaff et al. (2025a); H. Umeda et al. (2025) that the SEDs of LRDs generally appear similar to a blackbody at this wavelength range. This supports the interpretation of LRDs as an optically thick emission

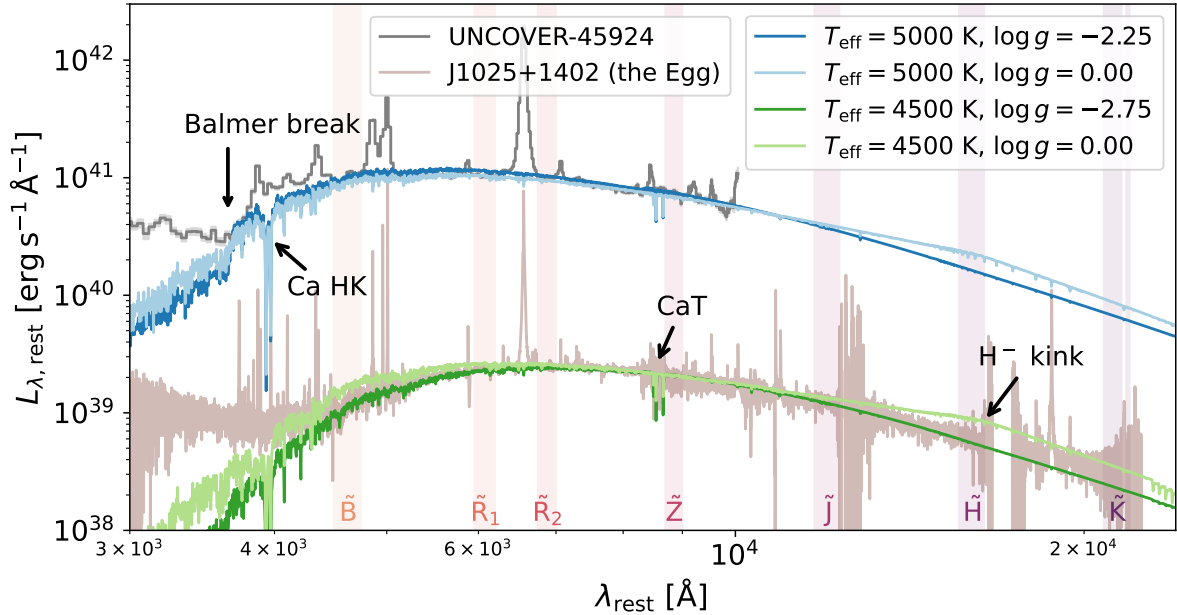


Figure 3. Overview of synthetic spectra and the spectral features to be discussed. Two models at $T_{\text{eff}} = 5000$ K broadly agree with the spectrum of UNCOVER-45924 (I. Labbé et al. 2024), but their different $\log g$ values give different Balmer break and Ca HK absorption strengths. Two models at $T_{\text{eff}} = 5000$ K broadly agree with the spectrum of J1025+1402 (nicknamed *the Egg*, X. Lin et al. 2025), but the low-gravity one gives a narrower optical-to-near-IR SED, stronger Ca II triplet (CaT) absorption, and does not show a continuum turnover at $\lambda_{\text{rest}} \sim 1.6 \mu\text{m}$ (the “ H^- kink”). The low-gravity model is preferred for *the Egg* if we account for the additional galaxy and dust emission (Section 5). All four models have $[\text{M}/\text{H}] = -1$ and $\xi_{\text{mtb}} = 2 \text{ km s}^{-1}$. The wavelength ranges of our synthetic photometry bands to be used later, from $\tilde{\text{B}}$ to $\tilde{\text{K}}$, are shaded in color.

medium with a narrow range of effective temperature in which the details of the inner energy source are largely hidden. However, beyond the zeroth-order agreement, models with different $\log g$ (atmosphere density) show distinct features in the continuum and lines. Figure 3 provides a roadmap to the following subsections, where we discuss the parametric dependence of various features.

We note that *the Egg* ($z_{\text{spec}} = 0.1007$, X. Lin et al. 2025; X. Ji et al. 2025a) is among the lowest-redshift LRDs known so far. It has the rare combined advantage of broad spectroscopic wavelength coverage and high spectral resolution. This object will be the main point of comparison in this section.

To quantify the SED profile, we design seven medium-width photometric bands with top-hat filters: $\tilde{\text{B}}$ (4500–4750 Å), $\tilde{\text{R}}_1$ (5950–6200 Å), $\tilde{\text{R}}_2$ (6750–7000 Å), $\tilde{\text{Z}}$ (8700–9000 Å), $\tilde{\text{J}}$ (11700–12300 Å), $\tilde{\text{H}}$ (15600–16400 Å), and $\tilde{\text{K}}$ (20800–21550, 21750–21900 Å), as indicated in Figure 3. We use the tilde symbol to avoid confusion with the standard broadband filters. The wavelengths are chosen to avoid strong emission or absorption lines. We measure the synthetic photometry for both our model spectra and real data in the following subsections.

4.1. Optical SED

We first focus on the overall shapes of our synthetic spectra. Recent demographic studies have quantified the optical-to-near-IR SED of LRDs in several ways, including fitting to a modified blackbody (A. de Graaff et al. 2025a) and to polynomials (G. Barro et al. 2025). We take a different approach and use colors to capture the optical and near-IR slopes. Two advantages of this representation are firstly, that the color measurement does not suffer from fitting systematics due to the inhomogeneous wavelength coverage of real data, and secondly, that our band coverage is designed to be relatively line-free and thus does not require the sometimes nontrivial task of masking lines.

We first study the wavelength range of approximately 4500–9000 Å, characterized by colors $\tilde{\text{B}}-\tilde{\text{R}}_1$ and $\tilde{\text{R}}_2-\tilde{\text{Z}}$. Figure 4 shows the color-color diagram of our synthetic spectra. To aid interpretation, we show the color temperatures on the top and right axes. For example, in the left panel, the point at $T_{\text{eff}} = 4500 \text{ K}$, $\log g = -2.0$, $\xi_{\text{mtb}} = 2 \text{ km s}^{-1}$ has $\tilde{\text{B}}-\tilde{\text{R}}_1 = 1.49$ and $\tilde{\text{R}}_2-\tilde{\text{Z}} = 0.43$; the corresponding color temperatures are $T_{\tilde{\text{B}}-\tilde{\text{R}}_1} = 3.4 \times 10^3 \text{ K}$ and $T_{\tilde{\text{R}}_2-\tilde{\text{Z}}} = 4.1 \times 10^3 \text{ K}$, i.e., a blackbody at $3.4 \times 10^3 \text{ K}$ or $4.1 \times 10^3 \text{ K}$ would have

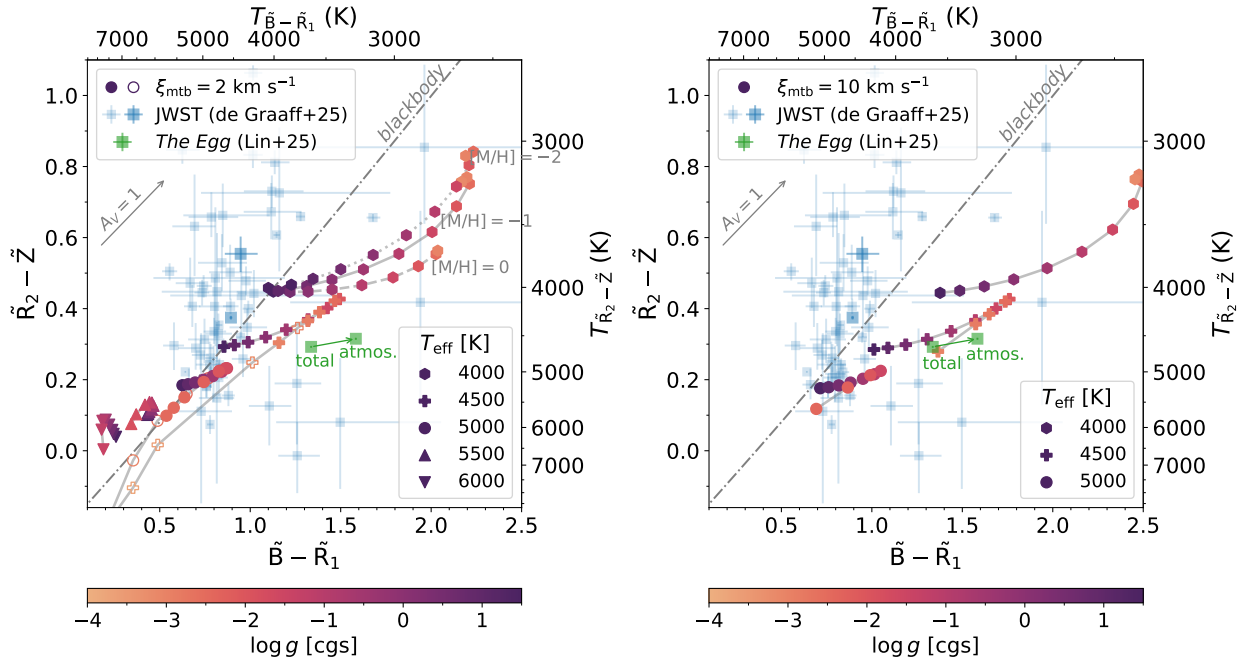


Figure 4. Color-color diagram of synthetic spectra (left: $\xi_{\text{mtb}} = 2 \text{ km s}^{-1}$; right: $\xi_{\text{mtb}} = 10 \text{ km s}^{-1}$) and observed LRDs. $\tilde{B} - \tilde{R}_1$ and $\tilde{R}_2 - \tilde{Z}$ (see Figure 3 and text for band definitions) capture the optical and near-IR slopes. Axes on the top and right give the color temperatures. Points below the dash-dotted “blackbody” line of $T_{\tilde{B}-\tilde{R}_1} = T_{\tilde{R}_2-\tilde{Z}}$ have SEDs narrower than a blackbody, i.e., with relatively red optical colors but blue near-IR colors. Gray vector indicates the change of colors by an SMC dust extinction of $A_V = 1$. Model points are color-coded by $\log g$; those with the same T_{eff} and $[M/H]$ are connected by gray lines. Three metallicity values are shown for $T_{\text{eff}} = 4000 \text{ K}$ and $\xi_{\text{mtb}} = 2 \text{ km s}^{-1}$, while only $[M/H] = -1$ is shown for other cases. Empty markers indicate no- g_{rad} models. The JWST LRD samples in A. de Graaff et al. (2025a) and the Egg (X. Lin et al. 2025) are shown in comparison; for the Egg, the “total” point measures the original spectrum and the “atmos.” point measures the spectrum subtracted by a best-fit young galaxy model (Section 5). For cool models with $T_{\text{eff}} < 5000 \text{ K}$, low- $\log g$ atmospheres may give SEDs significantly narrower than a blackbody.

the same $\tilde{B} - \tilde{R}_1$ or $\tilde{R}_1 - \tilde{Z}$ color as this model. Since $T_{\tilde{B}-\tilde{R}_1} < T_{\tilde{R}_1-\tilde{Z}}$, the SED of this model is narrower than a blackbody in the sense of having a relatively red optical color but a blue near-IR color. More generally, all points below the diagonal “blackbody” line, which delineates $T_{\tilde{B}-\tilde{R}_1} = T_{\tilde{R}_2-\tilde{Z}}$ (on which all perfect blackbodies would lie), have SEDs narrower than a blackbody, and vice versa. For $T_{\text{eff}} = 4000 \text{ K}$, a higher metallicity gives somewhat bluer colors at a given $\log g$ due to the backwarming effect of metal lines (e.g., B. Gustafsson et al. 1975), but this trend weakens at higher temperature, with a color change of no more than 0.03 mag between $[M/H] = 0$ and $[M/H] = -1$ for $T_{\text{eff}} = 5000 \text{ K}$. We do not show multiple metallicity values for higher T_{eff} for visual clarity.

Among the model points, low T_{eff} values unsurprisingly tend to give red optical and near-IR colors. Notably, the color temperatures do not always follow the effective temperature. When $T_{\text{eff}} < 5000 \text{ K}$, while models at $\log g \sim 1.5$ have $T_{\tilde{B}-\tilde{R}_1} \approx T_{\tilde{R}_2-\tilde{Z}} \approx T_{\text{eff}}$, lowering $\log g$ can reduce the color temperatures by more than 1000 K. $T_{\tilde{B}-\tilde{R}_1}$ is reduced more than $T_{\tilde{R}_2-\tilde{Z}}$, and the

SED becomes narrower than a blackbody at low $\log g$. This is because the absorption opacity at near-IR wavelengths, dominated by H^- , scales more steeply with density than the absorption opacity in the optical, which is dominated by metal lines. At low photosphere density, the optical opacity becomes comparatively larger than the near-IR opacity, and thus the optical continuum is produced further out in colder atmosphere layers. At very low $\log g$ (e.g., $\log g < -2$ for $T_{\text{eff}} = 4500 \text{ K}$), the colors start to move bluer at lower $\log g$ due to the increasing importance of the scattering opacity, which makes the continuum form at deeper, hotter layers than the Rosseland-mean photosphere. As for microturbulence, a comparison between the two panels in Figure 4 shows that a high ξ_{mtb} reddens the $\tilde{B} - \tilde{R}_1$ color and thus makes the SED narrower. This is due to metal absorption lines blending into a pseudo-continuum at blue optical wavelengths, and a high ξ_{mtb} promotes blending by boosting the line equivalent widths.

In comparison, we plot in Figure 4 the colors of JWST spectroscopically confirmed LRD samples from A. de Graaff et al. (2025a). We only include LRDs at redshifts

$z \lesssim 5$, whose \tilde{Z} bands are covered by JWST/NIRSpec. We calculate the colors using the PRISM spectra from the public Dawn JWST Archive, with the $1\text{-}\sigma$ uncertainties estimated from 1000 random draws of the error spectra. We similarly calculate the colors of *the Egg* using the spectral data reported in X. Lin et al. (2025).

We first note that a fraction of LRDs, including *the Egg*, show SEDs narrower than a blackbody; see also X. Lin et al. (2025); A. de Graaff et al. (2025a). This will be difficult to explain if one only assumes blackbody radiation. Dust extinction will not help: the vector of dust extinction (“ $A_V = 1$ ”, assuming a Small Magellanic (SMC)-averaged dust law, K. D. Gordon et al. 2024) is almost parallel to the “blackbody” line, which means that a dust-extincted blackbody is hardly narrower than a true blackbody in this color-color space. If we were to plot a line of blackbodies reddened by a generous $A_V = 3$, it would only be horizontally displaced from the “blackbody” line by < 0.2 mag. Moreover, there is mounting evidence for a physically distinct UV component of LRDs in addition to the atmosphere considered here (P. Rinaldi et al. 2024; C.-H. Chen et al. 2025b,a; G. Barro et al. 2025; J. F. W. Baggen et al. 2026), likely due to the host galaxy or a blue companion. Accounting for this component will intensify the narrowness. For example, if we subtract a young galaxy model from *the Egg* (to be described in Section 5), its location in color-color space will depart farther from the “blackbody” line (Figure 4) because the galaxy contributes significantly to the \tilde{B} band but much less so at longer wavelengths. Our synthetic spectra naturally reproduce narrow SEDs because of the radiative transfer effects described above.

On the other hand, many JWST data points are clustered at $T_{\tilde{B}-\tilde{R}_1} \sim 4500 - 5000$ K, with comparable or slightly lower $T_{\tilde{R}_2-\tilde{Z}}$, implying an SED shape comparable to or mildly broader than a blackbody. This agrees with the findings of A. de Graaff et al. (2025a). These samples appear to lie beyond our model points or suggest high $\log g$. An observational complication is that the atmospheres may have redder $\tilde{B} - \tilde{R}_1$ colors after subtracting the UV component. As a crude estimate, if the atmosphere contributes 60% and 80% of the total flux in the \tilde{B} and \tilde{R}_1 bands respectively (Figure 12 in W. Q. Sun et al. 2026), then the location of the intrinsic atmosphere in the color-color space will shift rightwards by $\Delta(\tilde{B} - \tilde{R}_1) = -2.5 \log(60\%/80\%) = 0.3$ mag. Even after this decomposition, the colors of some observed LRDs will still deviate from the models presented here. This indicates that a single optically thick atmosphere as considered in this work is too simplistic to explain the optical-to-near-IR colors of many LRDs. A range of atmosphere conditions in T_{eff} and/or $\log g$ may account

for a broad SED, in which case our models can provide a basis for constructing multi-component spectral fits. Indeed, a range of T_{eff} or $\log g$ is required to explain certain spectral features, e.g., the water absorption in B. Wang et al. (2026) and the smooth Balmer limit in R. E. Hviding et al. (2026). We caution that an alternative explanation for the observed broadness in SED is that the optical-to-near-IR continuum emission from LRDs is not fully optically thick (as in the “cocoon” scenario, A. Sneppen et al. 2026), in which case our models will cease to be applicable.

4.2. Near-IR SED

We have found in the previous section that our models naturally explain the optical SED of *the Egg*. Its rest-near-IR spectral coverage motivates us to investigate the SED at longer wavelengths. Moreover, inferring parameters such as $\log g$ from the optical alone is challenging: even without the uncertainty of host decomposition, degeneracy is severe as the colors non-monotonically change with $\log g$ and are sensitive to ξ_{mtb} . However, the near-IR SED can serve as an effective probe for $\log g$, as we show below.

Figure 5 presents the color-color space at longer wavelengths, around $6000 - 16000$ Å. Similarly to Figure 4, the color temperatures of the models can deviate drastically from T_{eff} , and smaller $\log g$ tends to give narrower SEDs (at least for hydrostatic cases). However, we highlight two important differences from the optical trends. First, for a given T_{eff} and $[M/H]$, there is an almost one-to-one mapping from $\log g$ to $\tilde{J} - \tilde{H}$ over a wide range of $\log g$. This trend is driven by the decreasing importance of the H^- opacity relative to the electron scattering opacity with decreasing atmosphere density. Second, this mapping is insensitive to ξ_{mtb} : the thin solid gray curves in Figure 5 almost overlap with the thick solid curves. This is because, unlike in the blue optical, atomic lines at this wavelength are too sparse to blend into a pseudo-continuum and affect the colors. These two advantages will allow us to put strong constraints on $\log g$ if the near-IR SED is available.

We now investigate what this implies for *the Egg*. In Figure 5, we show the measured near-IR colors from the observed spectrum (the “total” point). The point is located very close to the “blackbody” line. Meanwhile, on its left and right, the models with $4000 \text{ K} \leq T_{\text{eff}} \leq 5000 \text{ K}$ and $[M/H] = -1$ cross the “blackbody” line at $-2.5 < \log g < -2.0$. This suggests that $\log g < -2.0$ for *the Egg*. This can be even more stringent. Based on mid-IR photometry, X. Lin et al. (2025) found evidence for warm dust emission. Its high-frequency tail will enter the \tilde{H} band and make $\tilde{J} - \tilde{H}$ appear redder than

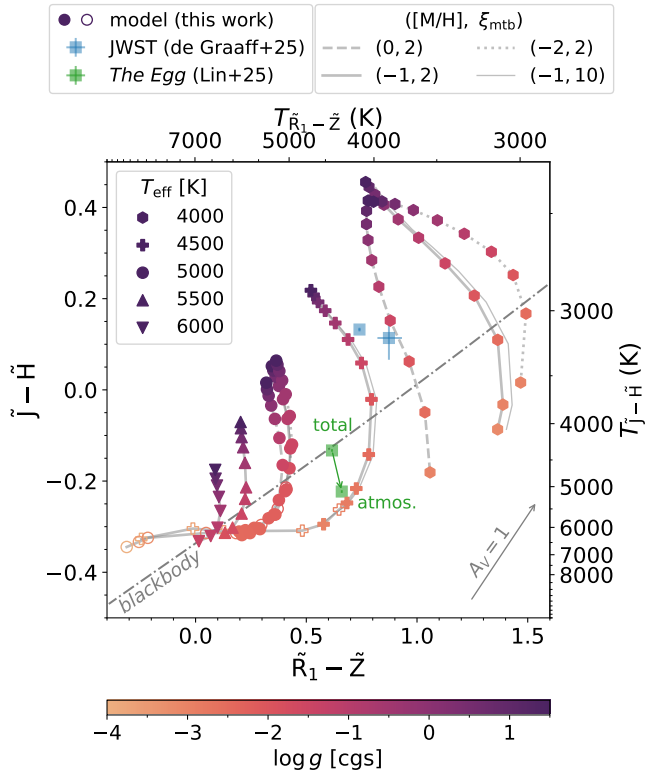


Figure 5. Similar to Figure 4, but for longer wavelengths, i.e., $\tilde{R}_1 - \tilde{Z}$ vs. $\tilde{J} - \tilde{H}$. Three metallicity values are shown for $T_{\text{eff}} = 4000, 5000$ K and $\xi_{\text{mtb}} = 2 \text{ km s}^{-1}$, while only $[M/H] = -1$ is shown for other cases. Microturbulence $\xi_{\text{mtb}} = 10 \text{ km s}^{-1}$ is shown as thin solid lines for $T_{\text{eff}} = 4000, 4500, 5000$ K and $[M/H] = -1$ but without markers for visual clarity. The JWST LRD samples in A. de Graaff et al. (2025a) and *the Egg* (X. Lin et al. 2025) are shown in comparison; for *the Egg*, the “total” point measures the original spectrum and the “atmos.” point measures the spectrum subtracted by a best-fit young galaxy model dominating in the UV and a warm dust emission model dominating in the mid-IR (Section 5). Model colors at long wavelengths strongly depend on $\log g$ and are insensitive to ξ_{mtb} ; the models suggest at least $\log g < -2$ for *the Egg*.

the intrinsic atmosphere. After subtracting the aforementioned galaxy component (which contributes 7% and 3% to the \tilde{R}_1 and \tilde{Z} band fluxes) and the dust emission component (which we model in Section 5, with results in agreement with X. Lin et al. 2025), we find that the intrinsic colors of *the Egg* (the “atmos.” point in Figure 5) are close to $T_{\text{eff}} = 4500$ K and $\log g = -2.85$. The “atmos.” point does not correct for potential dust extinction (see the “ $A_V = 1$ ” vector; not to be confused with dust emission), which would imply yet a narrower SED and a lower $\log g$. In conclusion, the strong, robust relation between $\log g$ and near-IR colors allows us to constrain at least $\log g < -2.0$ for *the Egg* or even ap-

proaching $\log g \approx -3$ when considering potential dust emission.

At higher redshifts, two LRDs in A. de Graaff et al. (2025a) have JWST/NIRSpec coverage of the \tilde{H} band. They are *the Rosetta Stone* (I. Juodžbalis et al. 2024) and GN-28074, highlighted with big blue squares in Figures 4 and 5. *The Rosetta Stone* has smaller error bars than GN-28074. Detailed modeling of these two objects is beyond the scope of this paper, but we note that *the Rosetta Stone* is closest to the model point at $T_{\text{eff}} = 4500$ K and $\log g = -1$, which is an upper limit since corrections for dust emission and/or extinction will imply even lower $\log g$. We will briefly discuss this object in Section 6.2.

Recently, A. Sneppen et al. (2026) reported cocoon models that partially reprocess an incident ionizing spectrum and reproduce many spectral features of LRDs. They predicted a near-IR spectral slope of $F_\lambda \propto \lambda^{-2}$, in better agreement with some LRDs than the Rayleigh-Jeans tail of a blackbody, $F_\lambda \propto \lambda^{-4}$. However, our optically thick atmosphere models are also redder than $F_\lambda \propto \lambda^{-4}$ (which has a very blue color of $\tilde{J} - \tilde{H} = -0.62$) and can predict a slope of $F_\lambda \propto \lambda^{-2}$ (corresponding to $\tilde{J} - \tilde{H} = 0.0$) for some combinations of T_{eff} and $\log g$. Therefore, the relatively red observed near-IR slopes may disfavor a simple Rayleigh-Jeans tail but do not rule out an optically thick atmosphere with more realistic radiative transfer. We will discuss how the cocoon and atmosphere scenarios may be distinguished in Section 6.2.

4.3. The H^- kink in the near-IR

The near-IR colors described above are related to a spectral feature at slightly longer wavelengths. In Figure 3, the synthetic spectra at $\log g = 0.00$ show a turnover at $\lambda \sim 1.6 \mu\text{m}$. We refer to this continuum feature as the “ H^- kink”: the wavelength corresponds to the ionization limit of the H^- ion, whose opacity increases at both shorter and longer wavelengths due to bound-free and free-free transitions, respectively (ch. 4-4, D. Mihalas 1978). When H^- is the dominant opacity source, it will shape the continuum to a redder slope at $\lambda < 1.6 \mu\text{m}$ but a bluer slope at $\lambda > 1.6 \mu\text{m}$, hence the kink shape.

To describe this kink, we use a spectral index,

$$m_{\text{kink}} \equiv 0.498m_J - m_H + 0.502m_K, \quad (7)$$

where m_J, m_H, m_K are the magnitudes of the \tilde{J}, \tilde{H} , and \tilde{K} bands defined at the beginning of Section 4. The coefficients are chosen such that a high m_{kink} corresponds to a high \tilde{H} -band flux relative to the two wings, while power-law SEDs of $F_\lambda \propto \lambda^0$ and $F_\lambda \propto \lambda^{-2}$ would give

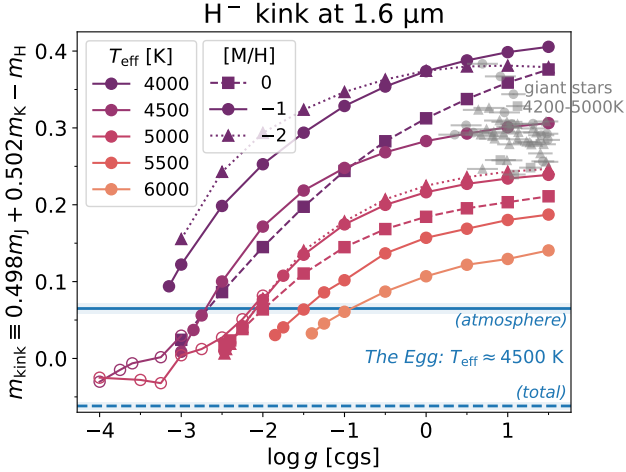


Figure 6. The continuum kink strength at $\lambda_{\text{rest}} \sim 1.6 \mu\text{m}$ due to H^- , defined in Equation (7). High values of the kink index m_{kink} corresponds to strong kinks. All models shown here have $\xi_{\text{mtb}} = 2 \text{ km s}^{-1}$ (m_{kink} is insensitive to ξ_{mtb}). The index of *the Egg*, measured from the observed spectrum directly (“total”) and from the spectrum with dust emission subtracted (“atmosphere”), are shown with horizontal dashed and solid blue lines, with the shade representing formal 1σ errors. Gray points show our kink measurements using the spectra of giant stars with $4200 \text{ K} \leq T_{\text{eff}} \leq 5000 \text{ K}$ and $\log g \leq 1.5$ (spectra from A. Gonneau et al. 2020; atmosphere parameter values and uncertainties from A. Arentsen et al. 2019), which are grouped into three metallicity bins, $-0.5 \leq [\text{Fe}/\text{H}] < 0.1$, $-1.5 \leq [\text{Fe}/\text{H}] < -0.5$, and $-2.6 < [\text{Fe}/\text{H}] < -1.5$, indicated by square, circle, and triangular markers respectively. Compared to stars at similar T_{eff} , *the Egg* ($T_{\text{eff}} \approx 4500 \text{ K}$) shows a much weaker kink, which suggests a very low atmosphere density, with $\log g \approx -3$, i.e., $\rho_{\text{ph}} \approx 10^{-11} \text{ g cm}^{-3}$ (Figure 2).

$m_{\text{kink}} = 0$. Figure 6 shows the index values of our model spectra. At a given T_{eff} , the kink strength increases with $\log g$. This is visually exemplified in Figure 3, with the kink apparent for the two high- $\log g$ spectra but not seen for those with lower $\log g$. The gravity dependence is because a low atmosphere density tends to suppress the H^- population by Saha equilibrium (D. Mihalas 1978). In addition, m_{kink} only weakly depends on metallicity at $T_{\text{eff}} = 5000 \text{ K}$. The metallicity will only introduce a scatter in $\log g$ by about one order of magnitude at a lower temperature of $T_{\text{eff}} = 4000 \text{ K}$, where the $[\text{M}/\text{H}] = 0$ curve shows a smaller index value than its lower-metallicity counterparts due to water absorption lines in the H band. We also check that m_{kink} is insensitive to ξ_{mtb} , which introduces a scatter in $\log g$ by < 0.1 dex at $T_{\text{eff}} \geq 4500 \text{ K}$ and $\log g < -1$. Overall, the kink can serve as a robust atmosphere density probe once T_{eff} is constrained from the overall SED.

To our knowledge, the only LRDs with spectra up to $\lambda_{\text{rest}} \sim 2 \mu\text{m}$ are the local ones reported in X. Lin et al. (2025). Long-wavelength spectroscopic coverage of high-redshift LRDs could test the optically thick atmosphere scenario on a demographic level, which we will discuss in Section 6.2. Now, we compare the kink index of *the Egg* with our models. Similarly to Section 4.2, we present two measurements, first using the observed spectrum as-is, then removing the best-fit warm dust emission (Section 5) from the spectrum to represent the intrinsic emission of the gas atmosphere. The results are shown as the “total” and “atmosphere” lines in Figure 6.

The kink in *the Egg* is remarkably weak, with $m_{\text{kink}} = -0.062^{+0.005}_{-0.004}$ for the “total” measurement and $m_{\text{kink}} = 0.065^{+0.007}_{-0.006}$ for the “atmosphere” value. As we have shown in Figures 3–5 and will further illustrate in Section 5, we need $T_{\text{eff}} \approx 4500 \text{ K}$ to explain the optical-to-near-IR colors of *the Egg*. Our model curve at this effective temperature only matches the intrinsic kink index at a very low $\log g \approx -3$. To further provide a stellar context, we measure the kink index of all stars in the second data release of the X-shooter Spectral Library (A. Gonneau et al. 2020) with atmosphere parameters in the range of $4200 \text{ K} \leq T_{\text{eff}} \leq 5000 \text{ K}$ and $\log g \leq 1.5$ (evaluated and cataloged in A. Arentsen et al. 2019). These stars span a metallicity range of $-2.6 < [\text{Fe}/\text{H}] < 0.1$ (A. Arentsen et al. 2019). All of the stars, with their relatively high gravity of $\log g > 0$, show strong kinks of $m_{\text{kink}} > 0.2$, in agreement with the model points of similar parameters, and in contrast to *the Egg*. We conclude that the lack of a kink feature in *the Egg* implies $\log g \ll 0$, i.e., a much lower photosphere density than those of giant stars.

4.4. The Balmer discontinuity

The Balmer break, or a spectral flux discontinuity at 3646 \AA , is a prominent continuum feature in many LRDs and motivated the interpretation of the emission as being due to a gas layer surrounding the black hole (K. Inayoshi & R. Maiolino 2025; X. Ji et al. 2025b; R. P. Naidu et al. 2025; D. J. Setton et al. 2024). H. Liu et al. (2025) have shown that, as a result of the density dependence of the opacity across the Balmer limit, an atmosphere density much lower than that of typical stars can produce a Balmer break at a cool temperature of $T_{\text{eff}} \sim 5000 \text{ K}$, thus reconciling the break feature and the intrinsically red rest-optical color of LRDs.

The same qualitative trend holds in the spectra in this work. In Figure 7, for the model spectra, we measure their Balmer break strengths defined as in H. Liu et al. (2025), i.e., the flux density (f_ν) ratio between two bands, $[4000, 4100] \text{ \AA}$ and $[3640, 3645] \text{ \AA}$. This definition

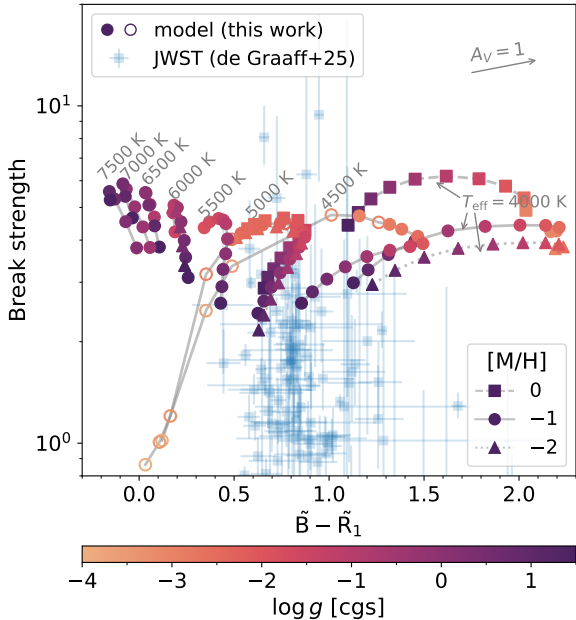


Figure 7. Balmer break strength and optical color of synthetic spectra and observed LRDs. Model points are color-coded by $\log g$; those with the same T_{eff} (annotated in gray) and $[M/H]$ are connected by gray lines. Only models with $\xi_{\text{mtb}} = 2 \text{ km s}^{-1}$ are shown here. The JWST LRD sample in A. de Graaff et al. (2025a) is shown in comparison. The model points will move down and approach the majority of the LRD data if there is a separate UV component contributing.

follows that used in A. de Graaff et al. (2025b,a) but uses a narrower blue band in order not to traverse the theoretical Balmer limit. For models with $T_{\text{eff}} \geq 4500 \text{ K}$, at a given T_{eff} , when $\log g$ decreases, the break strength first rises to a maximum before dropping. The maximum break strength is highest (~ 6) for $T_{\text{eff}} = 7000 \text{ K}$, whereas models with $T_{\text{eff}} = 4500 \text{ K} - 5500 \text{ K}$ have maximum break strengths at $\sim 4 - 5$. We note that this maximum is reached at a much lower $\log g$ for cool models. For example, the curve with $T_{\text{eff}} = 7500 \text{ K}$ peaks at $\log g = 1.0$, or $\rho_{\text{ph}} = 1.2 \times 10^{-10} \text{ g cm}^{-3}$; but for $T_{\text{eff}} = 4500 \text{ K}$, the location of the maximum shifts to $\log g = -3.25$, or $\rho_{\text{ph}} = 4 \times 10^{-12} \text{ g cm}^{-3}$. This agrees with the finding in H. Liu et al. (2025) that cool atmospheres can give a Balmer break at low density. At $T_{\text{eff}} = 4000 \text{ K}$, the measured break strength becomes dominated by the 4000 \AA break commonly seen in old galaxies rather than by the Balmer break itself.

Observationally, the break strengths of JWST samples in A. de Graaff et al. (2025a) span a wide range. One possible interpretation invokes varying contributions from the host galaxy (which would not exhibit a prominent Balmer break if actively forming stars) and

the atmosphere (G. Barro et al. 2025; W. Q. Sun et al. 2026). Under such an interpretation, the models presented here are compatible with break strengths at or below 4–5. However, the models fall below a few objects with the most extreme breaks (A. de Graaff et al. 2025b; R. P. Naidu et al. 2025). The models also show weaker breaks than our previous calculations in H. Liu et al. (2025) at optical colors comparable to most LRDs. We note that the predicted break strength is sensitive to the atmosphere temperature profile. Numerically, this work calculates thermal equilibrium more rigorously than H. Liu et al. (2025), where we used the gray atmosphere assumption and likely overestimated the break strength due to an overly cool upper atmosphere. Therefore, we conclude that 1D plane-parallel atmosphere models are compatible with most but not all of the Balmer breaks of LRDs. However, physically, this work only considers plane-parallel atmospheres, whereas a spherically extended atmosphere as in H. Liu et al. (2025) will naturally have cooler upper atmospheres due to geometric dilution and may have stronger breaks than in Figure 7.

Finally, in the bottom-left corner of Figure 7, our models with the lowest photosphere densities ($\rho_{\text{ph}} < 10^{-14} \text{ g cm}^{-3}$, or $\log g \sim -4$) show weak or even inverted breaks (Balmer jumps). This is physically possible in LTE models when the scattering opacity is important (A. Schuster 1905; A. B. Underhill 1949). Such a parameter space of low-density atmospheres may be relevant for objects such as the “X-Ray Dot” (R. E. Hviding et al. 2026), whose optical slope extends across the Balmer limit without signs of strong discontinuity.

4.5. Metal absorption lines

In our model spectra at $T_{\text{eff}} \sim 5000 \text{ K}$, the strongest metal absorption lines come from the Ca II ion, including the Ca H and K lines ($\lambda\lambda 3933, 3968 \text{ \AA}$) in the optical and the Ca triplet (CaT, $\lambda\lambda 8498, 8542, 8662 \text{ \AA}$) in the near-IR. These lines are well-known in stars at similar T_{eff} and have been identified in LRDs (I. Juodžbalis et al. 2024; X. Ji et al. 2025a; X. Lin et al. 2025). Notably, the CaT equivalent width (EW) strongly anticorrelates with surface gravity in the stellar regime and has been used as an atmosphere density probe (S. V. Mallik 1997; A. J. Cenarro et al. 2002; L. Mashonkina et al. 2007).

We measure the total absorption EW of the CaT from our model spectra, as shown in Figure 8. In the stellar regime, $\log g \gtrsim 0$, we recover the established relation that the EW decreases with $\log g$ at a given T_{eff} and $[M/H]$. As pointed out in U. G. Jorgensen et al. (1992); X. Lin et al. (2025), with a decreasing atmosphere density, the continuum opacity is diminished more strongly

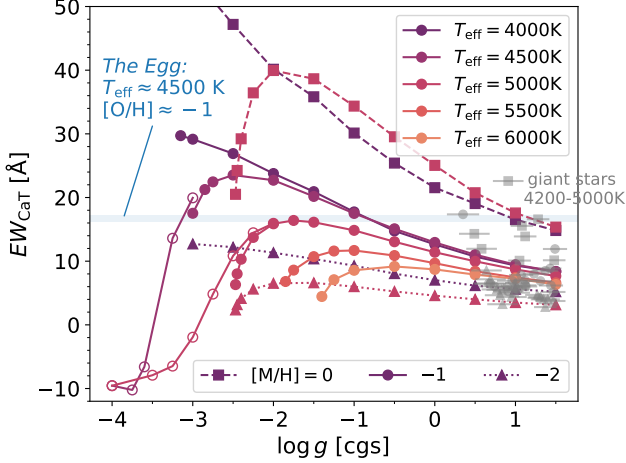


Figure 8. Total equivalent width of the CaT absorption lines ($\lambda\lambda 8498, 8542, 8662 \text{ \AA}$). Three metallicities, $[M/H] = 0, -1, -2$, are shown for $T_{\text{eff}} = 4000, 5000 \text{ K}$, while only one metallicity, $[M/H] = -1$, is shown for other values of T_{eff} . Only $\xi_{\text{mtb}} = 2 \text{ km s}^{-1}$ is shown, but $\xi_{\text{mtb}} = 10 \text{ km s}^{-1}$ gives almost the same result because the EW is mainly contributed by the line wings. The blue horizontal band indicates the measurement of *the Egg* (X. Lin et al. 2025). Gray points show our measured CaT EW of the same giant star sample as in Figure 6, but here we assume an α -element enhancement of 0.4 dex for stars with $[\text{Fe}/\text{H}] \leq -0.9$ and group them into metallicity bins of $-0.5 \leq [\alpha/\text{H}] < 0.1$ (square), $-1.5 \leq [\alpha/\text{H}] < -0.5$ (circle), and $-2.6 < [\alpha/\text{H}] < -1.5$ (triangle) to compare to models. The CaT EW depends on the atmosphere density and thus on $\log g$, and the EW of *the Egg* suggests $\log g \approx -3$ or -1 .

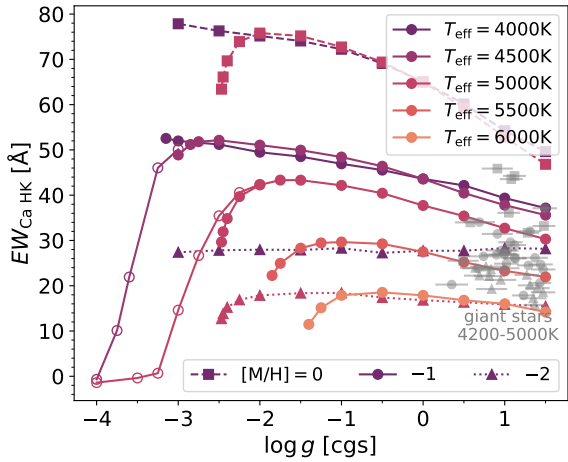


Figure 9. Same as Figure 8, but for the total equivalent width of the Ca H and K lines ($\lambda\lambda 3933, 3968 \text{ \AA}$).

than the CaT line opacity, leading to higher opacity contrast and thus higher EW. However, this trend reverses at very low $\log g$, and the CaT may even turn into emission ($EW_{\text{CaT}} < 0$). This is the regime where

the scattering opacity becomes important, which can induce emission lines even in an optically thick medium in LTE (A. Schuster 1905; A. B. Underhill 1949). Because of this downturn, weak or absent CaT absorption does not necessarily indicate extremely low metallicity.

Figure 8 indicates significant challenges in using CaT alone to constrain $\log g$. The EW is sensitive to both T_{eff} and $[M/H]$ besides $\log g$. Even if T_{eff} and $[M/H]$ are known a priori, two $\log g$ values may give the same EW due to the non-monotonic dependence of EW_{CaT} on $\log g$. For example, X. Lin et al. (2025) measured *the Egg* to have $EW_{\text{CaT}} = 16.7 \pm 0.5 \text{ \AA}$, as indicated in Figure 8; the gas-phase metallicity of the narrow line region has been independently measured as $[\text{O}/\text{H}] = -1.33 \pm 0.08, -1.21 \pm 0.08$ (Y. I. Izotov & T. X. Thuan 2008), -1.11 ± 0.03 (X. Lin et al. 2025), and $-0.96^{+0.21}_{-0.14}$ (X. Ji et al. 2025a) (we scaled the original measurements to a solar abundance of $12 + \log(\text{O}/\text{H}) = 8.69$ in M. Asplund et al. 2009). Assuming that the gas atmosphere of *the Egg* has a similar metallicity of $[M/H] = -1$, and taking $T_{\text{eff}} = 4500 \text{ K}$ from the SED shape of *the Egg*, we find that either $\log g = -3$ or $\log g = -1$ gives an EW_{CaT} value consistent with data. However, we will argue in Section 5 that we favor the $\log g = -3$ solution when combined with the continuum constraints. In either case, the EW_{CaT} value of *the Egg* is higher than that of most giant stars at comparable effective temperatures and Ca abundances (gray circle points), which supports a low-density regime of $\log g < 0$, as already argued in X. Lin et al. (2025).

We do a similar exercise for the total EW of the Ca HK lines, shown in Figure 9. The overall trend of the model spectra is similar to the CaT. Although the Ca HK lines have higher intrinsic EW than the CaT, the former are located at a shorter wavelength, where the host galaxy component and emission lines of LRDs likely bring significant infilling and complicate measurements in practice. We note that, without our implementation of partial frequency redistribution, the models would predict much broader HK lines, with the EW higher by 30% for the case of $T_{\text{eff}} = 5000 \text{ K}, \log g = -2.0, [M/H] = -1$ (Appendix A). Our treatment is still simplistic, and further development is needed (see, e.g., ch. 13, D. Mihalas 1978) to study the detailed profile of such strong resonance lines, especially near the line core.

5. APPLICATION TO A LOCAL LRD: THE CASE FOR LOW BLACK HOLE MASS

J1025+1402 (“*the Egg*”, $z_{\text{spec}} = 0.1007$, X. Lin et al. 2025; X. Ji et al. 2025a) is among the lowest-redshift LRDs known so far. In Section 4, we discussed several aspects of its spectral features, all of which point to a

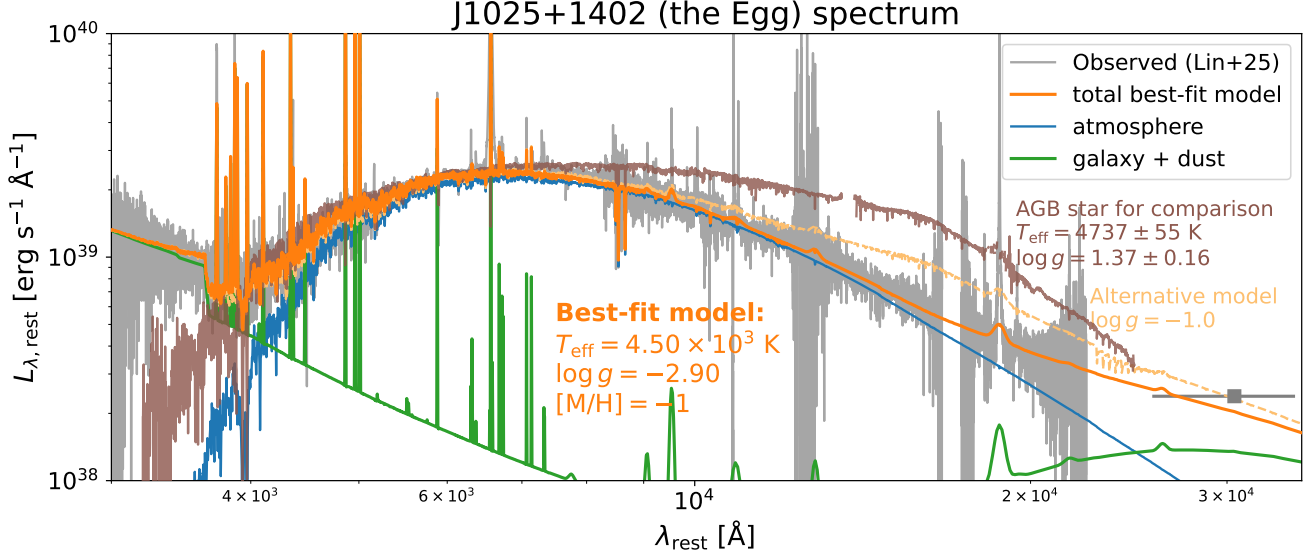


Figure 10. Composite model for *the Egg* compared to observation. The model consists of an atmosphere at $T_{\text{eff}} = 4.50 \times 10^3$ K, $\log g = -2.90$, $[M/H] = -1$ reddened by an SMC dust law at $A_V = 0.21$, a galaxy component, and a mid-infrared dust emission component. The low $\log g$ value is required by the narrow SED profile, the strong CaT absorption, and the lack of an H^- kink at $\lambda_{\text{rest}} \sim 1.6 \mu\text{m}$. In contrast, the low-resolution spectrum of an AGB star (CL* NGC 6121 LEE 4302, $T_{\text{eff}} = 4737 \pm 55$ K, $\log g = 1.37 \pm 0.16$, $[M/H] = -1.29 \pm 0.08$, A. Arentsen et al. 2019) has a much broader SED and stronger H^- kink, which is also true for our alternative optically thick atmosphere model at $\log g = -1$.

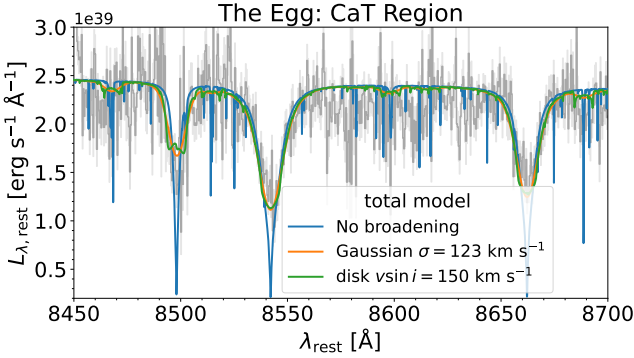


Figure 11. Same as Figure 10, but zoomed in to the CaT region. Three version of the model spectrum are shown: without broadening, with a Gaussian broadening with $\sigma = 123 \text{ km s}^{-1}$, and with a disk-geometry broadening with $v \sin i = 150 \text{ km s}^{-1}$. The two broadening scenarios give subtly different line profiles.

low-density atmosphere. In this section, we focus on this object as a case study. We will present our best-fit model in Section 5.1, where we bring together our previous analysis and highlight how a low $\log g$ simultaneously explains the narrow SED, the lack of a H^- kink, and the strong CaT absorption of *the Egg*. Then, in Section 5.2, we will interpret the low $\log g$ in terms of the atmosphere-scale total mass by outlining possible scenarios and discussing how to distinguish them in future modeling and observation.

5.1. Best-fit model and indications of low $\log g$

We construct a composite spectral model of *the Egg*. The total flux consists of three physical components:

1. An atmosphere model with T_{eff} , $\log g$, and ξ_{mtb} as free parameters. We fix $[M/H] = -1$ for simplicity, which broadly agrees with the gas-phase metallicities measured previously (Y. I. Izotov & T. X. Thuan 2008; X. Lin et al. 2025; X. Ji et al. 2025a). The atmosphere spectrum is convolved with a Gaussian kernel of $\sigma = 123 \text{ km s}^{-1}$ to match the CaT profile of the data. We predetermined σ by minimizing the χ^2 difference at $8450 \text{ \AA} < \lambda_{\text{rest}} < 8700 \text{ \AA}$ (i.e., the CaT region) between the normalized observed spectrum and an atmosphere model at $T_{\text{eff}} = 4500 \text{ K}$, $\log g = -3.0$, $[M/H] = -1$, $\xi_{\text{mtb}} = 2 \text{ km s}^{-1}$, which is close to our final best-fit result and has a CaT EW matching the data. Finally, we redden the spectrum by an SMC-averaged dust law (K. D. Gordon et al. 2024) at a visual extinction magnitude of A_V . The bolometric atmosphere luminosity before dust reddening is L_{atm} .
2. A host galaxy, constructed using the code FSPS (C. Conroy et al. 2009; C. Conroy & J. E. Gunn 2010; N. Byler et al. 2017). We assume a G. Chabrier (2003) initial mass function, a constant

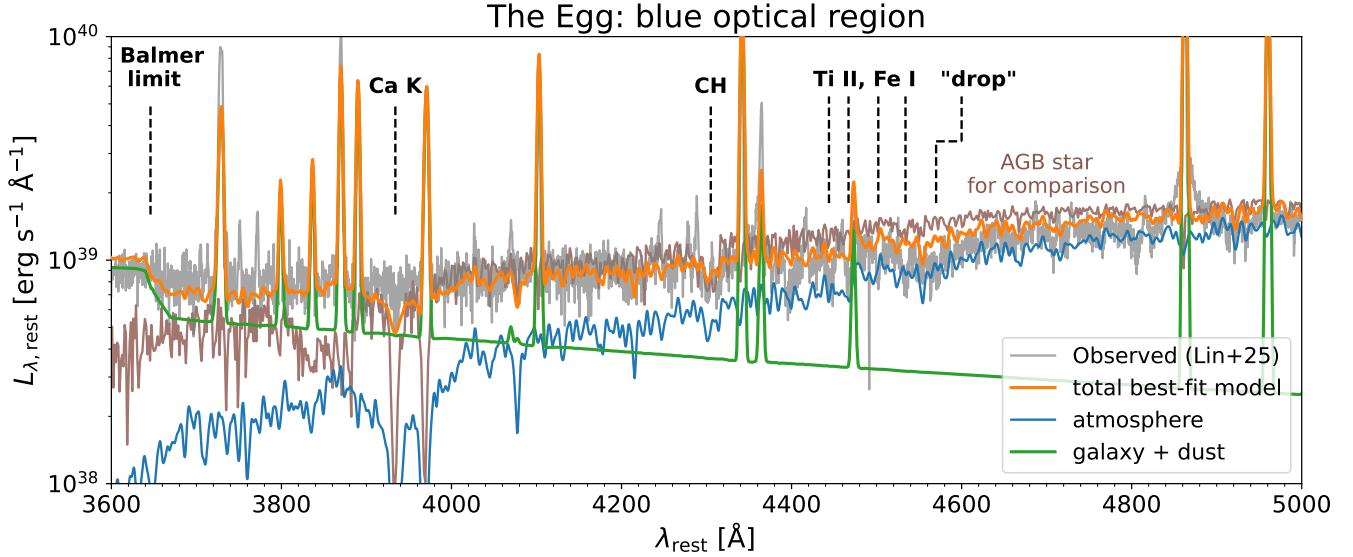


Figure 12. Same as Figure 10, but zoomed in to the blue optical region.

star formation rate⁵, and a fixed metallicity of $[M/H]_{\text{gal}} = -1$. The model is parameterized by the stellar age t_{gal} , the ionization parameter $\log U$ for the nebular emission, and the stellar mass M_* . We assume no dust extinction for the galaxy as implied by the very blue UV slope of *the Egg* and the narrow Balmer decrement being fully consistent with the intrinsic Case B prediction (X. Lin et al. 2025; X. Ji et al. 2025a).

3. Warm dust emission, modeled as a blackbody with a luminosity L_{dust} at a fixed $T_{\text{dust}} = 1038$ K. This approach follows X. Lin et al. (2025) (see also J. Lyu & G. H. Rieke 2021), who found that invoking a single blackbody temperature at 1038 K reasonably described the SED in the optical-to-near-IR. Colder dust is only important at longer wavelengths and is neglected here.

We have already argued in Section 4 that only a low- $\log g$ model can simultaneously account for the narrow near-IR SED, the lack of the H^- kink, and the strong CaT absorption. To verify our expectation and to ensure that we have not missed potential degeneracies, we perform Markov-Chain Monte Carlo (MCMC) fitting to find the best-fit parameters, which we describe in Appendix C. We emphasize that our MCMC posterior undoubtedly underestimates model systematics, so we refrain from interpreting the reported uncertainties. The purpose of our MCMC fitting is to identify the location and uniqueness of the best-fit solution with uninformed

⁵ We also explored using a τ -model for the star formation history and found that the best-fit τ far exceeded the stellar age.

Parameter	Prior	Best-fit
Atmosphere		
T_{eff} (K)	[4000, 5000]	4500
$\log(g/\text{cm s}^{-2})$	grid	-2.90
ξ_{mtb} (km s^{-1})	[2, 10]	4
A_V	[0, 3]	0.2
$\log(L_{\text{atm}}/\text{erg s}^{-1})$	[41, 45]	43.35
$[M/H]_{\text{atm}}$	-1 (fixed)	
Galaxy		
t_{gal} (Myr)	[1, 12]	1
$\log U$	[-4, -1]	-2.0
$\log(M_*/M_{\odot})$	[4, 9]	6.7
$[M/H]_{\text{gal}}$	-1 (fixed)	
Dust		
$\log(L_{\text{dust}}/\text{erg s}^{-1})$	[41, 45]	42.8
T_{dust} (K)	1038 (fixed)	
Uncertainty		
$\log s$	[-2, 1]	-1.1

Table 1. Free parameters in the composite model for *the Egg* and their best-fit values from the MCMC run. A “grid” prior for $\log g$ means the range is limited to the hydrostatic grid coverage in Figure 1. The uncertainty parameter $\log s$ is defined in Appendix C.

priors, which will support the robustness of a low $\log g$ for *the Egg*.

Table 1 summarizes the free parameters and their best-fit parameter values. Figure 10 shows our composite model of *the Egg*. The green curve here gives the galaxy and dust components, which we have used in Section 4. First, we highlight the narrowness of the

overall SED. In comparison, we plot the low-resolution spectrum of an Asymptotic Giant Branch (AGB) star, CL* NGC 6121 LEE 4302 (A. Gonneau et al. 2020), which has been inferred to have $T_{\text{eff}} = 4737 \pm 55$ K and $\log g = 1.37 \pm 0.16$ (A. Arentsen et al. 2019). Its SED shows a slightly bluer optical slope than *the Egg* but a dramatically redder color at $8000 - 16000$ Å. In the X-shooter Spectral Library, the spectra of other giant stars at comparable T_{eff} appear similar. Based on the trend in Figure 4, we propose a much lower $\log g$ than typical of giant stars to solve the narrowness problem. We reiterate that dust reddening or microturbulence will not significantly influence the near-IR narrowness; on the other hand, radiative transfer effects at low atmosphere density naturally give the narrow SED.

Another important distinction between the SEDs of *the Egg* and the AGB star is the strong H^- kink in the latter. In Figure 10, the slopes of the gray and brown curves are similar at ~ 2.0 μm , but the stellar SED visibly bends down at ~ 1.6 μm , while the SED of *the Egg* continues without an obvious change in slope. This illustrates their difference in the kink index in Figure 6. Again, a low value of $\log g = -3$ in our model suppresses the kink and gives a good agreement with data. This is the second piece of evidence for a low-density atmosphere.

Finally, we turn to the CaT absorption in *the Egg*. As we showed in Figure 8, the high CaT EW of this object, combined with $T_{\text{eff}} \approx 4500$ K and $[\text{M}/\text{H}] \approx -1$, suggests two gravity solutions: $\log g = -3$ and -1 . The orange curve in Figure 11, which includes the atmosphere at $\log g = -3$, illustrates the agreement of the model CaT EW with data⁶. We also explore the possibility of $\log g = -1$ by changing the atmosphere from $\log g = -3$ to -1 while keeping other parameters and components unchanged. The result is the yellow curve in the top panel. It shows a significantly worse match at the near-IR, with the SED being too broad and the kink feature too strong.

One may worry that inferring the intrinsic near-IR SED or the H^- kink strength of *the Egg* requires modeling of the warm dust emission (Figures 5 and 6), which remains uncertain. However, the dust correction works

in the opposite direction for the two probes. If dust emission were stronger than what we have found by MCMC, the intrinsic kink would be stronger and would suggest higher $\log g$, but meanwhile the $\tilde{\text{J}} - \tilde{\text{H}}$ color in Figure 5 would become bluer and would suggest even lower $\log g$, and vice versa. We do caution that when modeling CaT absorption, we assumed that the atmosphere metallicity of *the Egg* is similar to its gas-phase metallicity. If the metallicity is larger (smaller) the inferred $\log g$ would decrease (increase). Nevertheless, we stress that $\log g \approx -3$ can explain all the three spectral features discussed above. We note that the MCMC posterior touches the lower edge of $\log g$ in our model grid (Figure 16), which suggests that models at even lower $\log g$ beyond the grid coverage could potentially give similarly good fits.

As a side note, since our model atmospheres do not emit strongly at short wavelengths, the UV and the blue optical emission (up to $\lambda_{\text{rest}} \sim 4100$ Å) in our best-fit model for *the Egg* is dominated by the host galaxy, as shown in Figure 12. Nebular emission from the host galaxy produces a small inverse Balmer break (higher flux at shorter wavelengths), which is broadly consistent with the data, despite the Balmer break in the atmosphere model. The deep Ca HK absorption in the atmosphere is also almost completely veiled, only leaving visible a weak line core of Ca K, although it still appears somewhat stronger than data. As we noted in Section 4.5, our predictions near the Ca HK line cores are uncertain and require more detailed treatment. At longer wavelengths, the model reproduces the CH absorption feature at ~ 4305 Å, an atmospheric feature as argued in X. Ji et al. (2025a). The fitting is still imperfect: it underpredicts a series of Ti II and Fe I absorption lines, as well as the “drop” feature at ~ 4570 Å (X. Ji et al. 2025a). These features are also weak or absent from the spectrum of the AGB star. This suggests physical elements beyond the scope of this work, presumably gas absorption in the interstellar medium and/or turbulence in the atmosphere. We will further discuss the origin of the UV emission of LRDs in Section 6.2.

5.2. Interpretation

From Figure 2, $T_{\text{eff}} = 4500$ K and $\log g = -3$ (close to the best fit in Table 1) corresponds to $\rho_{\text{ph}} = 7 \times 10^{-12}$ g cm⁻³. As we argued in Section 2.1, the photosphere density is directly constrained by radiative transfer and is largely agnostic about dynamics. Indeed, the value of ρ_{ph} here agrees to within a factor of two with the one reported in X. Lin et al. (2025) (3.5×10^{-12} g cm⁻³), even though the earlier estimate did not assume hydrostatic equilibrium but instead was based on the super-

⁶ The CaT of *the Egg* is known to offset from the narrow emission lines by ~ -60 km s⁻¹ (X. Lin et al. 2025), so we shifted our model spectrum accordingly. In addition, the continuum flux in the data rises near the CaT region, and we are uncertain whether this is physical (e.g., from an extended atmosphere: see ch. 11-4, D. Mihalas 1978) or results from imperfect calibration at the edge of the spectrum. To focus on the line profile, we scaled up the model curve by 15% in the bottom panel to match the continuum of the data.

Eddington accretion model in H. Liu et al. (2025). In the following, we discuss a few possible scenarios that may give rise to the low inferred photospheric density and gravity $\log g$. We note in passing that independent of ρ_{ph} or $\log g$, the photosphere radius (or the scale of the effective emitting surface in scenarios without a spherical geometry) is $R_{\text{ph}} = \sqrt{L_{\text{atm}}/4\pi\sigma T_{\text{eff}}^4} = 8.7 \times 10^{15}$ cm, where we take $L_{\text{atm}} = 2.2 \times 10^{43}$ erg s $^{-1}$ and $T_{\text{eff}} = 4.50 \times 10^3$ K from Section 5.1.

First, we disfavor the possibility that $g_{\text{dyn}} = 0$, i.e., that the atmosphere of *the Egg* in fact satisfies radial hydrostatic equilibrium. Using $g_{\text{net}} = g = 10^{-3}$ cm s $^{-2}$ and applying Equation (6), we obtain the sum of the black hole and gas mass enclosed by the photosphere as $M_{\text{tot}} = 6 \times 10^2 M_{\odot}$. However, assuming no radial density inversion, a gas sphere of the size of the photosphere has a minimum mass of $M_{\text{gas,min}} = 4\pi\rho_{\text{ph}}R_{\text{ph}}^3/3 = 9.6 \times 10^3 M_{\odot} > M_{\text{tot}}$. We are then forced to invoke a gas shell whose radial thickness within the photosphere is limited to $\Delta R < 2 \times 10^{14}$ cm $\ll R_{\text{ph}}$ by the total mass.

The system can be less exotic if we relax the assumption of radial hydrostatic equilibrium and consider dynamical support due to bound motion of gas, i.e., $g_{\text{dyn}} > 0$ in Equation (1). In this case, we interpret the fitting results as $g_{\text{net}} = g - g_{\text{dyn}} \sim 10^{-3}$ cm s $^{-2}$. We refer to Equation (2) and estimate the value of dynamical acceleration g_{dyn} by

$$g_{\text{dyn}} = \frac{v_{\text{ph}}^2}{R_{\text{ph}}} = 1.1 \times 10^{-2} \text{ cm s}^{-2} v_{100}^2, \quad (8)$$

where v_{ph} is the characteristic velocity near the photosphere, and $v_{100} \equiv v_{\text{ph}}/(100 \text{ km s}^{-1})$. We see that $g_{\text{dyn}} \gg g_{\text{net}}$ for *the Egg* if $v \gg 30 \text{ km s}^{-1}$. With this, we substitute $g \approx g_{\text{dyn}}$ into the gravity term in Equation (6) and obtain

$$M_{\text{tot}} = 6.5 \times 10^3 M_{\odot} v_{100}^2. \quad (9)$$

This result does not depend on g_{net} itself other than the requirement of $g_{\text{dyn}} \gg g_{\text{net}}$. Therefore, the order of magnitude would remain correct even if g_{net} were larger by a factor of $\lesssim 10$.

The value of v_{ph} can be constrained using photospheric absorption lines depending on the nature of v_{ph} . The gas kinematics broadly falls into three categories: radial ordered motion, i.e., advection in the form of contraction/expansion or infall/outflow; azimuthal ordered motion, i.e., rotation; and chaotic motion. The first case can be probed by line offsets; the second and third cases by line broadening. The absorption lines in *the Egg* are offset from the narrow emission lines by -100 to -60 km s^{-1} (X. Lin et al. 2025), but it remains

unclear whether this blueshift is due to gas motion at the atmosphere or to a peculiar velocity between the black hole and the narrow line region. The line widths suggest a velocity on the same order: in Figure 11, we find that assuming chaotic gas motion (with the spectrum convolved by a Gaussian kernel)⁷ gives $\sigma = 123 \text{ km s}^{-1}$, while assuming rotational broadening of a disk annulus gives a line-of-sight velocity of $v \sin i = 150 \text{ km s}^{-1}$, where i is the inclination angle of the disk. Our σ is less than what one may naively infer from the FWHM ($441 \pm 18 \text{ km s}^{-1}$, X. Lin et al. 2025) because of the already large intrinsic line width (blue curve in Figure 11) required to explain the EW.

If the atmosphere is spherical, then we expect v_{ph} to be on the same order as the measured broadening. With $v_{\text{ph}} \sim 1.2 \times 10^2 \text{ km s}^{-1}$, Equation (9) implies that $M_{\text{tot}} \sim 1 \times 10^4 M_{\odot}$, on the same order as the gas mass $M_{\text{gas,min}}$. Therefore, this scenario features a small black hole mass, $M_{\text{BH}} \leq 1 \times 10^4 M_{\odot}$, and the gravity of the system may be dominated by the gas sphere instead of the black hole itself. Notably, the Eddington ratio of this system will be $\lambda_{\text{Edd}} = L_{\text{atm}}/L_{\text{Edd}}(M_{\text{BH}}) \geq 2 \times 10^1$. We also note that the dynamical timescale implied by the mass, $t_{\text{dyn}} \equiv \sqrt{R_{\text{ph}}^3/GM_{\text{tot}}} = 3 \times 10^1 \text{ yr } v_{100}^{-1}$, is longer than the rest-frame duration over which no strong variability is detected for *the Egg* ($\sim 5 \text{ yr}$ in the r band, C. J. Burke et al. 2025).

If, on the other hand, the atmosphere is in a disk geometry, then v_{ph} may be greater than the measured line-broadening velocity by a factor of $(\sin i)^{-1}$. This may allow for a much larger total mass. In addition, the minimum gas mass of the disk will likely be less than our previous estimate by a factor of the disk aspect ratio, leaving the black hole likely dominating the mass budget. Therefore, this disk scenario will have $M_{\text{BH}} \sim 1 \times 10^4 (\sin i)^{-2} M_{\odot}$, with the Eddington ratio $\lambda_{\text{Edd}} \sim 2 \times 10^1 (\sin i)^2$. Even so, we expect a lower limit on $\sin i$ at the disk aspect ratio $H/R \sim 0.1$ for a geometrically thin, perfectly face-on disk, which implies $M_{\text{BH}} \leq 1 \times 10^6 M_{\odot}$. The higher v_{ph} in this scenario would imply a shorter dynamical timescale, likely with an even shorter thermal timescale for a gravitationally unstable disk (T. A. Thompson et al. 2005), but whether variability at such timescales is observable depends on

⁷ This is known as ‘‘macroturbulence’’, which pertains to gas motion over a scale comparable to or larger than the photosphere scale height and is distinct from microturbulence ξ_{mtb} (e.g., D. F. Gray 1978). In practice, macroturbulence broadens the spectral flux and conserves line EWs, whereas microturbulence broadens the line opacity and in general changes the line EWs.

the number of embedded sources that power the disk emission, which is uncertain.

The sphere and disk scenarios may be observationally distinguishable from the line profiles, as shown in Figure 11 for the CaT. Disk rotation tends to produce double-peaked or boxy line profiles. This effect is most easily seen in relatively weak lines, e.g., the leftmost CaT line at $\lambda_{\text{rest}} = 8498 \text{ \AA}$. Future observation with a higher signal-to-noise ratio and spectral resolution may probe the detailed line shapes and directly constrain the atmosphere geometry. However, we caution that a lack of a double-peaked profile does not necessarily rule out the disk scenario if the disk is not geometrically thin or has optically thick winds (cf. the formation of single-peaked emission lines from disk winds in N. Murray & J. Chiang 1997).

The above constraint on g_{dyn} and hence on M_{tot} assumes that CaT absorption is cospatial with the photosphere. This is consistent with our model setup, where the atmosphere scale height is small relative to the photosphere radius (Equation (5)). If the atmosphere is extended in reality, with the line forming region located at a radius $R_{\text{CaT}} > R_{\text{ph}}$, the estimates in Equations (8)(9) will be greater by a factor of $R_{\text{CaT}}/R_{\text{ph}}$. However, CaT absorption requires dense gas at a relatively high temperature. The metastable 3d level of Ca II that gives the absorption needs to be collisionally populated by an electron density $n_e \gg n_{\text{crit}} \sim 10^7 \text{ cm}^{-3}$ (where the critical density is estimated from an Einstein A value of 0.9 s^{-1} of the 3d \rightarrow 4s transition and a collision strength of 4×10^0 ; data from the CHIANTI database, R. P. Dufresne et al. 2024, originally from M. Meléndez et al. 2007), which is not far from the LTE electron density at the photosphere ($n_e \sim 10^9 \text{ cm}^{-3}$ for gas at $T = 4500 \text{ K}$ and $\rho = 10^{-11} \text{ g cm}^{-3}$). Additionally, gas significantly colder than 4500 K cannot efficiently produce the absorption, as the CaT line opacity at LTE would decrease by a factor of 10 when $T = 3000 \text{ K}$. We thus deem it plausible that the CaT line is formed close to the continuum photosphere even if the atmosphere is extended, while acknowledging that the quoted M_{tot} is strictly a lower limit.

6. SUMMARY AND DISCUSSION

Understanding the nature of LRDs requires bridging the gap between detailed spectroscopic observations and theories attributing their optical-to-near-IR emission to an optically thick atmosphere. The commonly adopted blackbody approximation, while useful, misses spectral details that are essential for testing and applying these theories. To address this limitation, we construct a synthetic spectral library of optically thick atmospheres

over a parameter space tailored to LRDs, which we have made publicly available on GitHub (Section 1). We systematically explore the dependence of key continuum and line features on atmospheric parameters, most importantly the surface gravity (or, more precisely, the photospheric density; see Figure 2 and Section 2.1); then, applying the library to a local LRD, *the Egg*, we infer a low photospheric density $\rho_{\text{ph}} \sim 10^{-11} \text{ g cm}^{-3}$ (or $\log g \approx -3$) and hence a small total mass within the photosphere. This work provides a foundation for further tests of the optically thick atmosphere scenario and suggests a way of constraining the black hole mass within this picture. Our main conclusions are as follows.

1. The SEDs of optically thick atmospheres deviate from blackbodies. The optical and near-IR SEDs may appear broader or narrower than a blackbody, and the color temperatures may differ from T_{eff} by $> 1000 \text{ K}$ (Figures 4 and 5), depending on atmospheric parameters. Theoretical modeling of LRDs needs to consider radiative transfer effects instead of assuming simple blackbody emission.
2. The near-IR continuum provides useful constraints on photospheric density, i.e., on $\log g$. The $\tilde{J} - \tilde{H}$ color and the H^- kink strength increase monotonically with $\log g$, avoid the degeneracy from microturbulence, and are measurable from low-resolution spectroscopy (Figures 5 and 6; see also Figure 10).
3. Cool atmospheres ($4500 \leq T_{\text{eff}} \leq 6000 \text{ K}$) can produce a Balmer break at $\log g \ll 0$, with a peak break strength of 4 – 5 (Figure 7). The peak strength is consistent with most LRDs but falls short of those with the strongest breaks.
4. At a given T_{eff} and $[\text{M}/\text{H}]$, the EWs of the CaT and Ca HK absorption lines first increase and then decrease as $\log g$ becomes lower (Figures 8 and 9). Synthetic spectra at moderately low $\log g$ may give stronger EWs compared to the stellar regime ($\log g \gtrsim 0$), but those at very low $\log g$ show weak absorption or even emission.
5. The observed spectrum of *the Egg* appears narrower than a blackbody in the optical to near-IR (Figures 4 and 5), has a weak H^- kink (Figure 6), and shows strong CaT absorption for its metallicity (Figure 8). These are simultaneously explained by a low value of $\log g \approx -3$ at $T_{\text{eff}} = 4.50 \times 10^3 \text{ K}$, which yields a photosphere density of $\rho_{\text{ph}} \approx 10^{-11} \text{ g cm}^{-3}$ (Figure 2). This is corroborated by MCMC fitting to a composite model (Figure 10, Table 1).

6. We interpret the fitting result for *the Egg* as $\log g_{\text{net}} \approx -3$, which implies that the gravitational acceleration is mainly balanced by fluid motion, not pressure, with $g \approx g_{\text{dyn}} \gg g_{\text{net}}$ (Equation 8), where g_{dyn} is estimated from CaT absorption line broadening assuming that the line-forming region is cospatial with the photosphere. The inferred black hole mass is $M_{\text{BH}} \lesssim 1 \times 10^4 M_{\odot}$ in a spherical geometry or $M_{\text{BH}} \lesssim 1 \times 10^6 M_{\odot}$ in a face-on disk geometry, which corresponds to Eddington ratios $\lambda_{\text{Edd}} = L_{\text{atm}}/L_{\text{Edd}} \geq 20$ and $\lambda_{\text{Edd}} \geq 0.2$ respectively (Section 5.2). The constraints on the black hole mass are lower limits if the CaT absorption lines are produced exterior to the continuum photosphere.

6.1. Caveats and future directions for modeling

Our spectral library does not explain all features of LRDs and does not necessarily apply to all (or any!) LRDs. Our calculations are designed for atmospheres with sufficiently high optical depth, whose deep layers thermalize any radiation and keep atomic level populations at LTE.⁸ The inference of $\log g$ is based on the optically thick assumption. Such atmospheres in our current framework do not explain the broad Balmer emission lines. Our synthetic spectra also have difficulty reproducing the strongest observed Balmer breaks of LRDs. However, one important feature of optically thick atmospheres is that they robustly predict many spectral features and correlations between them that can be used to test the model (just as in stars). In addition, the optically thick atmosphere model naturally produces narrow continuum SEDs, as is strikingly seen in *the Egg*.

The optically thick atmosphere can be contrasted with the “cocoon envelope” scenario (R. P. Naidu et al. 2025; V. Rusakov et al. 2026; Y. Asada et al. 2026; A. Sneppen et al. 2026), which features a gas layer that partially reprocesses ionizing incident radiation and produces broad emission lines in situ. In this case, the radiation and level populations throughout the gas layer can be markedly different from LTE and are not described by the models in this paper. However, the optically thick atmosphere and the cocoon are not mutually exclusive. Our models have higher photosphere volume and column densities ($n_{\text{H}} \sim 10^{12} \text{ cm}^{-3}$ and $N_{\text{H}} \sim 10^{27} \text{ cm}^{-2}$ in the best-fit model for *the Egg*) than typical cocoon models

(e.g., $n_{\text{H}} \sim 10^{10} \text{ cm}^{-3}$ and $N_{\text{H}} \sim 10^{24-26} \text{ cm}^{-2}$ in A. Sneppen et al. 2026), but our fitting does not rule out a low n_{H} since we have not fully covered that part of the parameter space (e.g., $\log g \ll -3$ at $T_{\text{eff}} < 4500 \text{ K}$) due to convergence issues. Furthermore, the cocoon model spectra in A. Sneppen et al. (2026) with the highest column densities have already become optically thick in the Balmer continuum (evidenced by their strong Balmer breaks) and moderately so in the optical (evidenced by their continuum becoming reminiscent of a blackbody and their Ca HK absorption). The cocoon picture at still higher values of n_{H} and/or N_{H} will likely smoothly connect to our LTE optically thick atmosphere regime. It would be very valuable to quantitatively explore this transition in order to test both models against LRD observations. In addition, while the cocoon models reproduce the broad emission lines, the spectra in A. Sneppen et al. (2026) still require substantial dust extinction ($A_V > 1 \text{ mag}$; their Figure B8) to reproduce the observed variety of SED curvature in the optical, especially at the narrow end. We speculate that a wide range of volume and/or column densities spanning the optically thick atmosphere regime and the cocoon regime may simultaneously show broad emission lines and a narrow SED. Future demographic studies in the rest-near-IR may further test which regime is more applicable to the continuum, which we will discuss in Section 6.2.

The optically thick atmosphere is inherent in various physical pictures of LRDs, such as quasi-stars (M. C. Begelman & J. Dexter 2025; A. D. Santarelli et al. 2025), spherical super-Eddington accretion flows (H. Liu et al. 2025), supermassive stars (D. Nandal & A. Loeb 2026), and gravitationally unstable disks (C. Zhang et al. 2025; L. Zwick et al. 2025; Y.-X. Chen et al. 2026). For example, A. D. Santarelli et al. (2025) predicted $\log g < 0$ from their quasi-star models, but they used stellar synthetic spectra at $\log g = 0$ because lower $\log g$ were then unavailable. Our spectral library, which covers the parameter space of their model LRDs, can be directly incorporated into their framework and indeed into future modeling works.

Within the regime of the optically thick atmosphere, we have conducted (admittedly limited) tests on non-LTE effects and found only mild deviations from the LTE synthetic spectra. We calculate non-LTE level populations for H, Mg, and Ca in two cases, $\log g = 0$ and -2 (with $T_{\text{eff}} = 5000 \text{ K}$, $[\text{M}/\text{H}] = -1$, $\xi_{\text{mtb}} = 2 \text{ km s}^{-1}$). Compared to LTE, all photometric band magnitudes differ by less than 0.03 mag, and the Balmer break strength and the CaT EW are enhanced by $< 1.5\%$ and $< 12\%$ in both cases. This agrees with previous calculations showing weak non-LTE effects on the CaT in the stel-

⁸ This is similar to what is termed the “blackbody envelope” scenario of LRDs in Y. Asada et al. (2026), although we refer to our model the “optically thick atmosphere” because (a) we have shown that the spectrum of an optically thick atmosphere has features deviating from a blackbody, and (b) our model is not limited to a spherical geometry.

lar regime (U. G. Jorgensen et al. 1992; L. Mashonkina et al. 2007; T. Merle et al. 2011). We caution that our tests are restricted in allowing only a few species to have non-LTE populations and in fixing the density and temperature to the LTE profile. In addition, we still assume an LTE number density for H^- . P. S. Barklem & A. M. Amarsi (2024) recently evaluated non-LTE effects of H^- for stars and found a $< 1\%$ difference in the optical continuum for $T_{\text{eff}} \leq 5000$ K and $\log g \geq 1$, with a tendency to overpopulate H^- compared to LTE. If this tendency holds at lower $\log g$, we will expect the H^- opacity to be more manifest in non-LTE (e.g., stronger kinks), which will strengthen our conclusion about the low $\log g$ of *the Egg*. An even greater uncertainty is that the predicted spectra may be modified by additional physics, e.g., photoionization by massive stars in the vicinity or shock heating due to accretion, which have been suggested as potential origins of emission lines for LRDs (J. F. W. Baggen et al. 2024; Y. Asada et al. 2026; Y.-X. Chen et al. 2026).

We have made several simplifications about the gas distribution in our atmosphere models. The 1D model neglects spatial inhomogeneity and requires simplified treatments such as mixing-length convection and microturbulence. The plane-parallel geometry will break down for extended atmospheres. The dynamical implications of gas motion are only considered in an order-of-magnitude fashion. Multi-dimensional radiation hydrodynamic simulations will be needed to capture these complications self-consistently, and our calculations provide a baseline for comparison with future, more dynamically realistic models. In the alternative cocoon scenario, simulations could clarify the formation mechanism and stability of the gas cocoon and connect it to the accretion process of the black hole.

6.2. Future directions for observation

Throughout this work, we have chosen *the Egg* as a key observational point of comparison. The near-IR spectral coverage up to $\lambda_{\text{rest}} \sim 2 \mu\text{m}$ is crucial in our inference of $\log g$ (via the $\tilde{J} - \tilde{H}$ color and the H^- kink strength). In addition, the high-resolution, high signal-to-noise ratio spectrum of metal absorption lines, in particular the CaT, provides additional evidence for a low $\log g$ and enables us to constrain the dynamical acceleration g_{dyn} via line broadening. The resulting atmosphere-scale total mass we find for *the Egg* is $\sim 10^{4-6} M_{\odot}$, with the lower value applying in a spherical model and the higher value applying for a face-on disk. The black hole mass can be two orders of magnitude lower than that inferred from virial scaling relations ($10^{6.5} M_{\odot}$, X. Lin et al. 2025). A similar deviation has been suggested for

many high-redshift LRDs based on detailed modeling of the broad emission lines (V. Rusakov et al. 2026; R. P. Naidu et al. 2025; S.-J. Chang et al. 2026; A. Torralba et al. 2025; A. Sneppen et al. 2026), although debates remain (I. Juodžbalis et al. 2024; M. Brazzini et al. 2025, 2026). Future analysis of the broad emission lines of *the Egg* may provide independent constraints on its central engine. Our estimate for *the Egg* suggests a rapidly accreting black hole in the intermediate mass regime, which, if further confirmed, will have profound implications for the demographics and evolutionary history of massive black holes.

The methodology here in principle can be applied to JWST LRDs at higher redshifts under the assumption that the optical-to-near-IR emission arises from an optically thick atmosphere, albeit with large uncertainties due to the currently limited spectroscopic wavelength coverage and the scarcity of high-frequency-resolution data. In the case of *the Rosetta Stone*, we have inferred $\log g \leq -1.0$ in Section 4.2; this implies $M_{\text{tot}} \leq 8 \times 10^5 M_{\odot} (L_{\text{atm}}/3 \times 10^{44} \text{ erg s}^{-1})(T_{\text{eff}}/4500 \text{ K})^{-4}$ assuming radial hydrostatic equilibrium (Equation (6)), but we caution that (a) here we have no strong constraints on g_{dyn} , which is important in the case of *the Egg*; and (b) the reference value of the atmosphere luminosity $3 \times 10^{44} \text{ erg s}^{-1}$ is measured directly from the spectrum at $3600 \text{ \AA} < \lambda_{\text{rest}} < 16700 \text{ \AA}$ without correcting for dust extinction or subtracting the UV or dust emission components.

Even before attempting to infer the black hole mass for individual JWST samples, one may first want to test whether the optically thick assumption holds on the population level. A prediction of the optically thick atmosphere scenario is a population-wise correlation between $\tilde{J} - \tilde{H}$ and m_{kink} since both increase with the $\log g$ parameter, as shown in Figure 13. Furthermore, presuming that g_{net} correlates with M_{BH} and that M_{BH} correlates with bolometric luminosity, we expect more luminous LRDs to appear broader in the near-IR SED, have redder $\tilde{J} - \tilde{H}$, and show stronger kinks. This trend can be distinguished from the prediction currently presented in A. Sneppen et al. (2026), which generally shows a power-law near-IR SED with a typical slope of $F_{\lambda} \propto \lambda^{-2}$ (diamond symbol in Figure 13),⁹ although we caution that dust emission may weaken the observed kink strength (as in our model for *the Egg*).

⁹ A. Sneppen et al. (2026) noted that they currently did not include the H^- opacity in their calculation, so the predictions are not strictly comparable. However, the lower typical gas density in their model likely makes H^- less important than in our models.

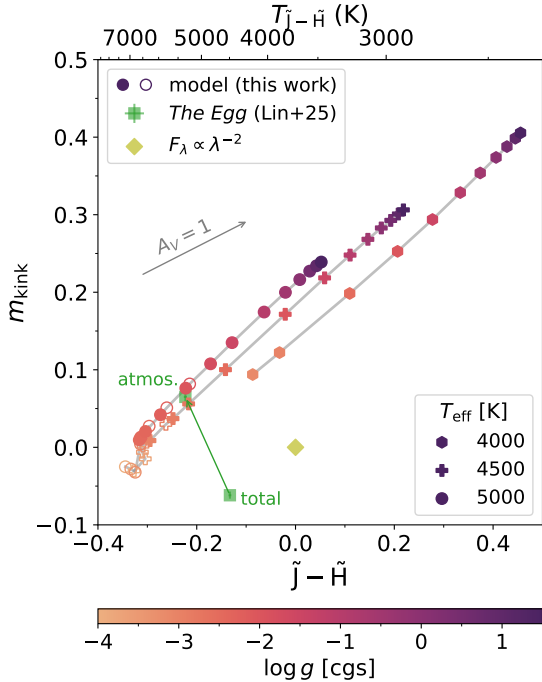


Figure 13. Relation between the near-IR color and the H⁻ kink strength, similar to Figure 5. Only models with $[M/H] = -1$ and $\xi_{\text{mtb}} = 2 \text{ km s}^{-1}$ are shown. The measurement for *the Egg* is shown in comparison, where the “total” point measures the original spectrum and the “atmos.” point measures the spectrum subtracted by a best-fit young galaxy model dominating in the UV and a warm dust emission model dominating in the mid-IR (Section 5). Gray vector indicates the change by an SMC dust extinction of $A_V = 1$. The optically thick atmosphere scenario predicts a correlation between $\bar{J} - \bar{H}$ and m_{kink} for the LRD population, which may be distinguished from a power-law SED $F_\lambda \propto \lambda^{-2}$.

Future observations could allow more conclusive modeling for high-redshift LRDs. First, a JWST/MIRI spectroscopic survey could cover the near-IR continuum including the kink feature at $z > 2$, where most known LRDs are located. The near-IR continuum could test the optically thick scenario (Figure 13). If confirmed, joint modeling of dust and atmosphere emission can be used to measure $\log g_{\text{net}}$ as we have done for *the Egg*. Second, high-resolution spectroscopy aimed at potential absorption lines, e.g., the CaT, could simultaneously constrain g_{dyn} from line broadening and g_{net} from line EWs. A combination of these two observations could give a black hole mass measurement independent of the one from emission lines. Our work also motivates the search for more low-redshift LRDs, whose rest-near-IR

spectra are accessible with JWST/NIRSpec or even by ground-based IR telescopes, as is the case in X. Lin et al. (2025). A larger sample size could address whether the atmospheric condition of *the Egg* is common or special.

The optically thick atmosphere models in this work do not emit strongly in the UV, which necessitated the galaxy component in our fitting of *the Egg* to dominate the UV and blue optical. This is compatible with the spatially resolved UV emission of some LRDs (P. Rinaldi et al. 2024; C.-H. Chen et al. 2025b,a) and the scarcity of evidence for short-term UV variability (M. Kokubo & Y. Harikane 2024; Z. Zhang et al. 2025a), and similar scenarios have been considered in some demographic studies of LRDs (e.g., G. Barro et al. 2025; W. Q. Sun et al. 2026). However, it remains possible that the central engine contributes to the UV, as in the cocoon scenario at relatively low column density (A. Sneppen et al. 2026). In addition, a nearby blue companion could supply part of the UV flux in a subset of LRDs (J. F. W. Baggen et al. 2025, 2026). Future image decomposition analysis and variability monitoring of LRDs will bring a more comprehensive understanding of the entire SED.

ACKNOWLEDGMENTS

HL thanks Ivan Hubeny for providing the water line list used in this work and for technical help. HL thanks Rohan Naidu, Anna de Graaff, David Setton, and Bingjie Wang for constructive discussions. The calculations presented in this article were performed on computational resources managed and supported by Princeton Research Computing, a consortium of groups including the Princeton Institute for Computational Science and Engineering (PICSciE) and the Office of Information Technology’s High Performance Computing Center and Visualization Laboratory at Princeton University. The Center for Computational Astrophysics at the Flatiron Institute is supported by the Simons Foundation.

Software: Astropy (Astropy Collaboration et al. 2013, 2018, 2022), corner.py (D. Foreman-Mackey 2016), emcee (D. Foreman-Mackey et al. 2013), FSPS (C. Conroy et al. 2009; C. Conroy & J. E. Gunn 2010; N. Byler et al. 2017), Matplotlib (J. D. Hunter 2007), Numpy (C. R. Harris et al. 2020), Pyphot (M. Fouesneau 2025), Scipy (P. Virtanen et al. 2020), TLUSTY (I. Hubeny 1988; I. Hubeny et al. 2021)

APPENDIX

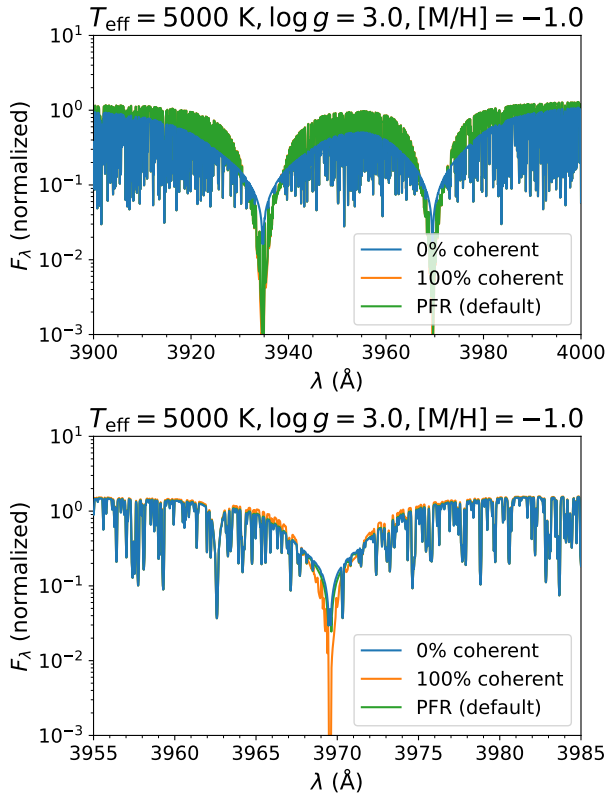


Figure 14. Effect of partial redistribution (PFR). Three cases are compared: treating the Ca HK line opacity as pure absorption (blue), pure scattering (orange), and a PFR treatment (green, the default in this work). Top: a low-gravity model. The PFR result closely aligns with the pure scattering case (the green line almost perfectly overlaps the orange), which predicts much narrower line profiles than the pure absorption case. Bottom: a high-gravity model (zoomed in on the Ca H line). The PFR result now more resembles the pure absorption case.

A. PARTIAL FREQUENCY REDISTRIBUTION OF CA H AND K LINES

Stellar atmosphere models usually assume that the emission and absorption of photons in a bound-bound transition are independent. This will become inaccurate if, after an atom or ion absorbs a line photon and becomes radiatively excited, it has a significant probability of immediately re-emitting the photon by radiatively decaying to the original state. In this case, the frequencies of the absorbed and re-emitted photons become correlated, which requires the treatment known as partial frequency redistribution (PFR).

PFR in the form of the “partial coherent scattering approximation” has been implemented in TLUSTY for Lyman- α and the resonance lines of Mg I and II and in SYNSPEC for Lyman- α (I. Hubeny & T. Lanz 2017, Appendix F). We similarly implement PFR in SYNSPEC for

the Ca HK lines. In brief, in the line wing (more than three Doppler widths away from the line center), we model a fraction of the line opacity as coherent scattering. We evaluate this coherence fraction at each spatial location,

$$\gamma_{\text{coh}} = \frac{\Gamma_R}{\Gamma_R + \Gamma_{\text{Stark}} + \Gamma_{\text{vdW}}}, \quad (\text{A1})$$

where Γ_R , Γ_{Stark} , and Γ_{vdW} are the natural, Stark, and van der Waals damping parameters of the line. Physically, Γ_{Stark} and Γ_{vdW} characterize the elastic collision rates of the excited Ca II ion with electrons and neutral hydrogen, which will lead to decoherence if they are much greater than the radiative decay rate, Γ_R . In the line core (less than three Doppler widths from the line center), we no longer introduce coherent scattering, which becomes negligible due to thermal frequency redistribution (J. T. Jefferies & O. R. White 1960). We note that PFR is only relevant for resonance lines. For subordinate lines, such as the CaT, the excited state is far more likely to branch out to other channels of radiative decay (by emitting an H or K line photon in the case of Ca II) than to re-emit coherently.

In Equation (A1), Γ_{Stark} and Γ_{vdW} are proportional to the electron and neutral hydrogen density, respectively, so we expect atmospheres with low $\log g$ (and therefore low photosphere density) to have higher γ_{coh} . Figure 14 shows the Ca HK profile with γ given by Equation (A1) compared to setting $\gamma_{\text{coh}} = 0$ or $\gamma_{\text{coh}} = 1$ everywhere in the atmosphere. For $T_{\text{eff}} = 5000$ K, $\log g = -2$, $[M/H] = -1$, the PFR result is almost identical to the case with 100% coherent scattering due to the low collision rates. In contrast, in the model with $\log g = 3$, the much higher atmosphere density brings the PFR result closer to the case with $\gamma_{\text{coh}} = 0$. We note that the usual implicit assumption of $\gamma_{\text{coh}} = 0$ in stellar models will predict extremely broad absorption wings at low $\log g$, with a total EW of the Ca HK lines higher by 30% than the PFR treatment.

As a caveat, we still assume that the Ca II level population satisfies LTE although PFR is essentially a non-LTE effect. Our treatment should be viewed as a first-order non-LTE correction to the LTE model; a fully self-consistent calculation will need to further account for statistical equilibrium. In addition, predicting the detailed line profile will likely require sophisticated frequency redistribution functions (ch. 13, D. Mihalas 1978), although coherent scattering is a good approximation in the far wing (J. T. Jefferies & O. R. White 1960), which contributes most of the EW in low- $\log g$ models.

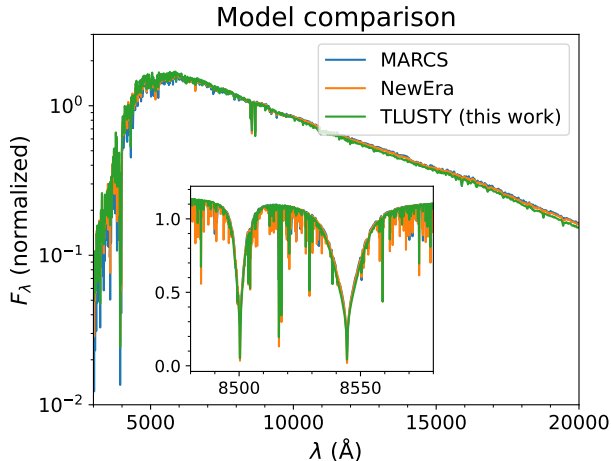


Figure 15. Comparison of synthetic spectrum in this work and two previously published stellar models. The parameters are $T_{\text{eff}} = 5000$ K, $\log g = 0$, $[M/H] = 0$. The inset figure shows two of the CaT lines. Our result agrees with the published models in the overall SED and the CaT line profiles.

B. COMPARISON WITH EXISTING SYNTHETIC STELLAR SPECTRA

We test that our spectra calculated using TLUSTY agree with widely used theoretical spectral libraries in the stellar regime. Figure 15 compares one example from our grid at $T_{\text{eff}} = 5000$ K, $\log g = 0$, $[M/H] = 0$ with spectra at the same parameter from two stellar grids in the literature, MARCS (B. Gustafsson et al. 2008) and NewEra (P. H. Hauschildt et al. 2025). We find good agreement among the three spectra, with the continua different by $\lesssim 10\%$ in the optical and $\lesssim 5\%$ in the near-IR. Their absorption profiles of the CaT are also consistent, as shown in the inset. We note that MARCS and the current NewEra grid assume LTE, as in this work, but they use a spherical geometry designed for typical stellar radii. The atomic data are also different. These may explain the minor differences in the results.

C. MCMC FITTING FOR *the Egg*

In this section, we describe our MCMC fitting methods and the results. As we have cautioned in the main text, the purpose of this exercise is to identify the global best fit and rule out potential degeneracies by scanning the parameter space. We refrain from interpreting the

posteriors from the MCMC, which likely underestimate parameter uncertainties due to model systematics.

We use uniform priors for all parameters as listed in Table 1. We limit the parameter range of $\log g$ within our hydrostatic grid. We rebin the data and model spectra into 200 logarithmically equally spaced wavelength bins in $3200 \text{ \AA} < \lambda_{\text{rest}} < 22300 \text{ \AA}$. We also evaluate the synthetic photometry of the redshifted model spectrum in the WISE W1 band. The total logarithmic likelihood is given by

$$\ln P = -\frac{1}{2} \sum_{\text{bin}} \left[\frac{(L_{\lambda,\text{data}} - L_{\lambda,\text{model}})^2}{\sigma_{\lambda,\text{data}}^2 + s^2 L_{\lambda,\text{model}}^2} + \ln(\sigma_{\lambda,\text{data}}^2 + s^2 L_{\lambda,\text{model}}^2) \right], \quad (\text{C2})$$

where the sum goes over all the spectral wavelength bins (except for bins with strong emission lines in the data, which we mask off) and the W1 photometric band. The errors have two components: $\sigma_{\lambda,\text{data}}$ comes from the spectral errors propagated through rebinning or from the WISE photometry, and s is a free parameter representing the unknown relative systematic uncertainties in the model. We note that Equation (C2) assumes that the errors in each bin are uncorrelated. This is the motivation of our rebinning the spectrum to low resolution: we found that the residuals would be strongly correlated if we directly used the original, high-resolution spectrum, which would result in severely overconfident posteriors. Therefore, we reduce the number of bins to 200, by which the residuals have a correlation length close to one bin (i.e., statistically uncorrelated). Rebinning also implies that we are mainly fitting the continuum shape rather than individual lines. However, rebinning does not strongly influence the best-fit parameter values.

Figure 16 shows the MCMC posterior of the atmosphere parameters and the uncertainty parameter. The best-fit is unique, and the posterior shows no sign of multi-modality. We further experimented artificially inflating the error at all wavelength bins by 10 to flatten the posterior, but still found no multi-modality. This supports the robustness of our inference of a low $\log g$. We also note that the best-fit $\log s$ implies that the average disagreement between the model-data is $\lesssim 10\%$, which suggests reasonably good model performance.

REFERENCES

Akins, H. B., Casey, C. M., Lambrides, E., et al. 2024, arXiv e-prints, arXiv:2406.10341, doi: 10.48550/arXiv.2406.10341

Ananna, T. T., Bogdán, Á., Kovács, O. E., Natarajan, P., & Hickox, R. C. 2024, ApJL, 969, L18, doi: 10.3847/2041-8213/ad5669

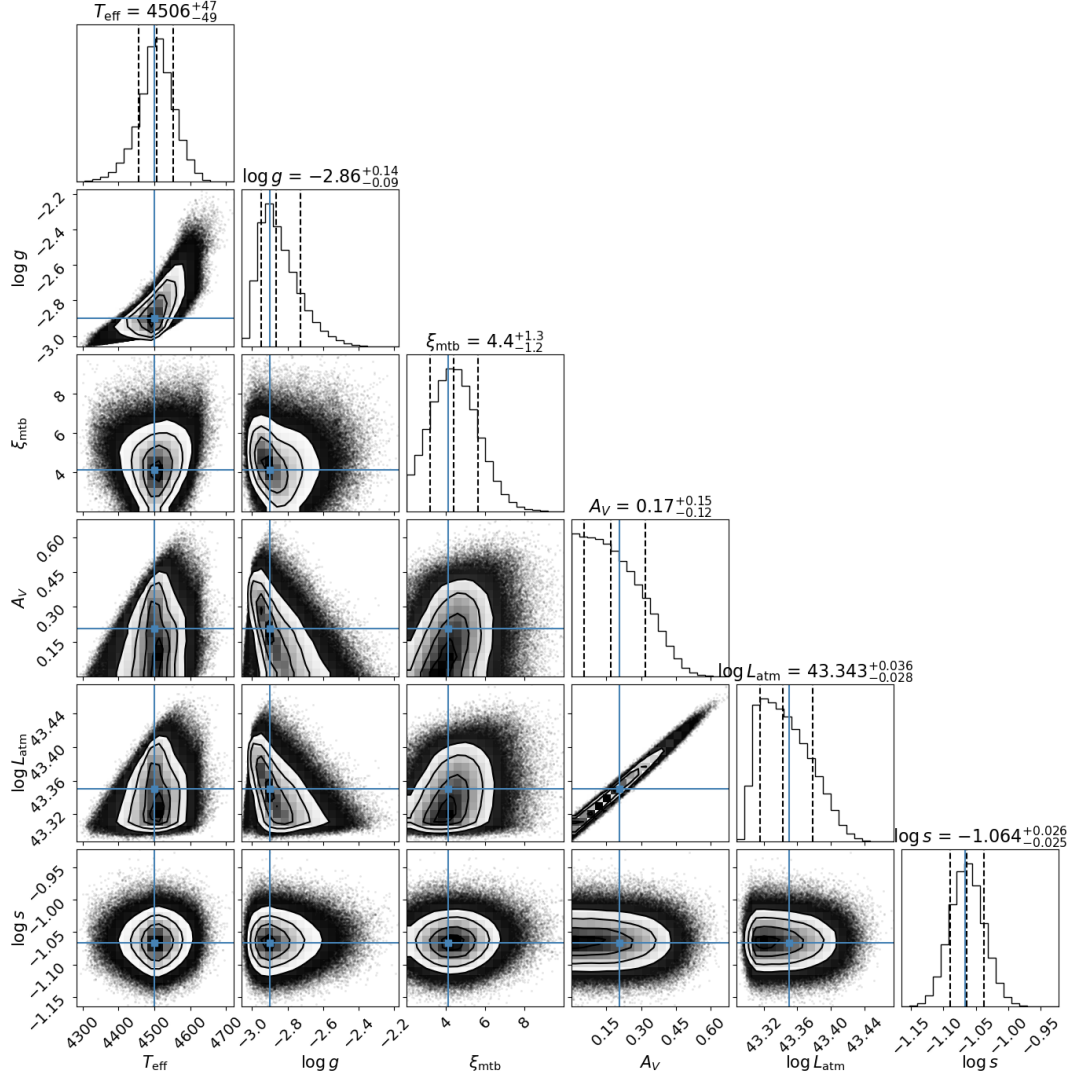


Figure 16. Corner plot of the MCMC posterior sample. Only parameters related to the atmosphere are shown.

Arentsen, A., Prugniel, P., Gonneau, A., et al. 2019, *A&A*, 627, A138, doi: [10.1051/0004-6361/201834273](https://doi.org/10.1051/0004-6361/201834273)

Asada, Y., Inayoshi, K., Fei, Q., Fujimoto, S., & Willott, C. 2026, arXiv e-prints, arXiv:2601.10573, doi: [10.48550/arXiv.2601.10573](https://doi.org/10.48550/arXiv.2601.10573)

Asplund, M., Grevesse, N., Sauval, A. J., & Scott, P. 2009, *ARA&A*, 47, 481, doi: [10.1146/annurev.astro.46.060407.145222](https://doi.org/10.1146/annurev.astro.46.060407.145222)

Astropy Collaboration, Robitaille, T. P., Tollerud, E. J., et al. 2013, *A&A*, 558, A33, doi: [10.1051/0004-6361/201322068](https://doi.org/10.1051/0004-6361/201322068)

Astropy Collaboration, Price-Whelan, A. M., Sipőcz, B. M., et al. 2018, *AJ*, 156, 123, doi: [10.3847/1538-3881/aabc4f](https://doi.org/10.3847/1538-3881/aabc4f)

Astropy Collaboration, Price-Whelan, A. M., Lim, P. L., et al. 2022, *ApJ*, 935, 167, doi: [10.3847/1538-4357/ac7c74](https://doi.org/10.3847/1538-4357/ac7c74)

Baggen, J. F. W., Scoggins, M. T., van Dokkum, P., et al. 2026, arXiv e-prints, arXiv:2602.02702, doi: [10.48550/arXiv.2602.02702](https://doi.org/10.48550/arXiv.2602.02702)

Baggen, J. F. W., van Dokkum, P., Labbé, I., & Brammer, G. 2025, arXiv e-prints, arXiv:2512.03239, doi: [10.48550/arXiv.2512.03239](https://doi.org/10.48550/arXiv.2512.03239)

Baggen, J. F. W., van Dokkum, P., Brammer, G., et al. 2024, *ApJL*, 977, L13, doi: [10.3847/2041-8213/ad90b8](https://doi.org/10.3847/2041-8213/ad90b8)

Barklem, P. S., & Amarsi, A. M. 2024, *A&A*, 689, A100, doi: [10.1051/0004-6361/202451157](https://doi.org/10.1051/0004-6361/202451157)

Barro, G., Perez-Gonzalez, P. G., Kocovski, D., et al. 2025, arXiv e-prints, arXiv:2512.15853, doi: [10.48550/arXiv.2512.15853](https://doi.org/10.48550/arXiv.2512.15853)

Begelman, M. C., & Dexter, J. 2025, arXiv e-prints, arXiv:2507.09085, doi: [10.48550/arXiv.2507.09085](https://doi.org/10.48550/arXiv.2507.09085)

- Brazzini, M., D'Eugenio, F., Maiolino, R., et al. 2025, arXiv e-prints, arXiv:2507.08929, doi: [10.48550/arXiv.2507.08929](https://doi.org/10.48550/arXiv.2507.08929)
- Brazzini, M., D'Eugenio, F., Maiolino, R., et al. 2026, arXiv e-prints, arXiv:2601.22214, doi: [10.48550/arXiv.2601.22214](https://doi.org/10.48550/arXiv.2601.22214)
- Burke, C. J., Stone, Z., Shen, Y., & Jiang, Y.-F. 2025, arXiv e-prints, arXiv:2511.16082, doi: [10.48550/arXiv.2511.16082](https://doi.org/10.48550/arXiv.2511.16082)
- Byler, N., Dalcanton, J. J., Conroy, C., & Johnson, B. D. 2017, *ApJ*, 840, 44, doi: [10.3847/1538-4357/aa6c66](https://doi.org/10.3847/1538-4357/aa6c66)
- Casey, C. M., Akins, H. B., Finkelstein, S. L., et al. 2025, arXiv e-prints, arXiv:2505.18873, doi: [10.48550/arXiv.2505.18873](https://doi.org/10.48550/arXiv.2505.18873)
- Cenarro, A. J., Gorgas, J., Cardiel, N., Vazdekis, A., & Peletier, R. F. 2002, *MNRAS*, 329, 863, doi: [10.1046/j.1365-8711.2002.05029.x](https://doi.org/10.1046/j.1365-8711.2002.05029.x)
- Chabrier, G. 2003, *PASP*, 115, 763, doi: [10.1086/376392](https://doi.org/10.1086/376392)
- Chang, S.-J., Gronke, M., Matthee, J., & Mason, C. 2026, *MNRAS*, 545, staf2131, doi: [10.1093/mnras/staf2131](https://doi.org/10.1093/mnras/staf2131)
- Chen, C.-H., Ho, L. C., Li, R., & Inayoshi, K. 2025a, arXiv e-prints, arXiv:2505.03183, doi: [10.48550/arXiv.2505.03183](https://doi.org/10.48550/arXiv.2505.03183)
- Chen, C.-H., Ho, L. C., Li, R., & Zhuang, M.-Y. 2025b, *ApJ*, 983, 60, doi: [10.3847/1538-4357/ada93a](https://doi.org/10.3847/1538-4357/ada93a)
- Chen, K., Li, Z., Inayoshi, K., & Ho, L. C. 2025, arXiv e-prints, arXiv:2505.22600, <https://arxiv.org/abs/2505.22600>
- Chen, Y.-X., Liu, H., Li, R., et al. 2026, arXiv e-prints, arXiv:2602.06954, doi: [10.48550/arXiv.2602.06954](https://doi.org/10.48550/arXiv.2602.06954)
- Conroy, C., & Gunn, J. E. 2010, *ApJ*, 712, 833, doi: [10.1088/0004-637X/712/2/833](https://doi.org/10.1088/0004-637X/712/2/833)
- Conroy, C., Gunn, J. E., & White, M. 2009, *ApJ*, 699, 486, doi: [10.1088/0004-637X/699/1/486](https://doi.org/10.1088/0004-637X/699/1/486)
- de Graaff, A., Hviding, R. E., Naidu, R. P., et al. 2025a, arXiv e-prints, arXiv:2511.21820, doi: [10.48550/arXiv.2511.21820](https://doi.org/10.48550/arXiv.2511.21820)
- de Graaff, A., Rix, H.-W., Naidu, R. P., et al. 2025b, arXiv e-prints, arXiv:2503.16600, doi: [10.48550/arXiv.2503.16600](https://doi.org/10.48550/arXiv.2503.16600)
- Dufresne, R. P., Del Zanna, G., Young, P. R., et al. 2024, *ApJ*, 974, 71, doi: [10.3847/1538-4357/ad6765](https://doi.org/10.3847/1538-4357/ad6765)
- Foreman-Mackey, D. 2016, *Journal of Open Source Software*, 1, 24, doi: [10.21105/joss.00024](https://doi.org/10.21105/joss.00024)
- Foreman-Mackey, D., Hogg, D. W., Lang, D., & Goodman, J. 2013, *PASP*, 125, 306, doi: [10.1086/670067](https://doi.org/10.1086/670067)
- Fouesneau, M. 2025, pyphot_v2.0.0 Zenodo, doi: [10.5281/zenodo.14712174](https://doi.org/10.5281/zenodo.14712174)
- Gonneau, A., Lyubenova, M., Lançon, A., et al. 2020, *A&A*, 634, A133, doi: [10.1051/0004-6361/201936825](https://doi.org/10.1051/0004-6361/201936825)
- Gordon, K. D., Fitzpatrick, E. L., Massa, D., et al. 2024, *ApJ*, 970, 51, doi: [10.3847/1538-4357/ad4be1](https://doi.org/10.3847/1538-4357/ad4be1)
- Gray, D. F. 1978, *SoPh*, 59, 193, doi: [10.1007/BF00951830](https://doi.org/10.1007/BF00951830)
- Gustafsson, B., Bell, R. A., Eriksson, K., & Nordlund, A. 1975, *A&A*, 42, 407
- Gustafsson, B., Edvardsson, B., Eriksson, K., et al. 2008, *A&A*, 486, 951, doi: [10.1051/0004-6361:200809724](https://doi.org/10.1051/0004-6361:200809724)
- Harris, C. R., Millman, K. J., van der Walt, S. J., et al. 2020, *Nature*, 585, 357, doi: [10.1038/s41586-020-2649-2](https://doi.org/10.1038/s41586-020-2649-2)
- Hauschildt, P. H., Barman, T., Baron, E., Aufdenberg, J. P., & Schweitzer, A. 2025, *A&A*, 698, A47, doi: [10.1051/0004-6361/202554171](https://doi.org/10.1051/0004-6361/202554171)
- Hayashi, C. 1961, *PASJ*, 13, 450
- Hubeny, I. 1988, *Computer Physics Communications*, 52, 103, doi: [10.1016/0010-4655\(88\)90177-4](https://doi.org/10.1016/0010-4655(88)90177-4)
- Hubeny, I., Allende Prieto, C., Osorio, Y., & Lanz, T. 2021, arXiv e-prints, arXiv:2104.02829, doi: [10.48550/arXiv.2104.02829](https://doi.org/10.48550/arXiv.2104.02829)
- Hubeny, I., Blaes, O., Krolik, J. H., & Agol, E. 2001, *ApJ*, 559, 680, doi: [10.1086/322344](https://doi.org/10.1086/322344)
- Hubeny, I., & Hubeny, V. 1998, *ApJ*, 505, 558, doi: [10.1086/306207](https://doi.org/10.1086/306207)
- Hubeny, I., & Lanz, T. 2017, arXiv e-prints, arXiv:1706.01935, doi: [10.48550/arXiv.1706.01935](https://doi.org/10.48550/arXiv.1706.01935)
- Hui, Y., Krolik, J. H., & Hubeny, I. 2005, *ApJ*, 625, 913, doi: [10.1086/429884](https://doi.org/10.1086/429884)
- Hunter, J. D. 2007, *Computing in Science & Engineering*, 9, 90, doi: [10.1109/MCSE.2007.55](https://doi.org/10.1109/MCSE.2007.55)
- Hviding, R. E., de Graaff, A., Liu, H., et al. 2026, arXiv e-prints, arXiv:2601.09778, doi: [10.48550/arXiv.2601.09778](https://doi.org/10.48550/arXiv.2601.09778)
- Inayoshi, K., & Ho, L. C. 2025, arXiv e-prints, arXiv:2512.03130, doi: [10.48550/arXiv.2512.03130](https://doi.org/10.48550/arXiv.2512.03130)
- Inayoshi, K., & Maiolino, R. 2025, *ApJL*, 980, L27, doi: [10.3847/2041-8213/adaebd](https://doi.org/10.3847/2041-8213/adaebd)
- Izotov, Y. I., & Thuan, T. X. 2008, *ApJ*, 687, 133, doi: [10.1086/591660](https://doi.org/10.1086/591660)
- Jefferies, J. T., & White, O. R. 1960, *ApJ*, 132, 767, doi: [10.1086/146980](https://doi.org/10.1086/146980)
- Ji, X., D'Eugenio, F., Juodžbalis, I., et al. 2025a, arXiv e-prints, arXiv:2507.23774, doi: [10.48550/arXiv.2507.23774](https://doi.org/10.48550/arXiv.2507.23774)
- Ji, X., Maiolino, R., Übler, H., et al. 2025b, arXiv e-prints, arXiv:2501.13082, doi: [10.48550/arXiv.2501.13082](https://doi.org/10.48550/arXiv.2501.13082)
- Jiang, Y.-F., Cantiello, M., Bildsten, L., Quataert, E., & Blaes, O. 2015, *ApJ*, 813, 74, doi: [10.1088/0004-637X/813/1/74](https://doi.org/10.1088/0004-637X/813/1/74)
- Jorgensen, U. G., Carlsson, M., & Johnson, H. R. 1992, *A&A*, 254, 258

- Juodžbalis, I., Ji, X., Maiolino, R., et al. 2024, MNRAS, 535, 853, doi: [10.1093/mnras/stae2367](https://doi.org/10.1093/mnras/stae2367)
- Kido, D., Ioka, K., Hotokezaka, K., Inayoshi, K., & Irwin, C. M. 2025, arXiv e-prints, arXiv:2505.06965, doi: [10.48550/arXiv.2505.06965](https://doi.org/10.48550/arXiv.2505.06965)
- King, A. 2024, MNRAS, 531, 550, doi: [10.1093/mnras/stae1171](https://doi.org/10.1093/mnras/stae1171)
- Kocevski, D. D., Onoue, M., Inayoshi, K., et al. 2023, ApJL, 954, L4, doi: [10.3847/2041-8213/ace5a0](https://doi.org/10.3847/2041-8213/ace5a0)
- Kokubo, M., & Harikane, Y. 2024, arXiv e-prints, arXiv:2407.04777, doi: [10.48550/arXiv.2407.04777](https://doi.org/10.48550/arXiv.2407.04777)
- Kurucz, R. L. 1979, ApJS, 40, 1, doi: [10.1086/190589](https://doi.org/10.1086/190589)
- Kurucz, R. L. 2019, <http://kurucz.harvard.edu/linelists/>
- Labbé, I., van Dokkum, P., Nelson, E., et al. 2023, Nature, 616, 266, doi: [10.1038/s41586-023-05786-2](https://doi.org/10.1038/s41586-023-05786-2)
- Labbe, I., Greene, J. E., Matthee, J., et al. 2024, arXiv e-prints, arXiv:2412.04557, doi: [10.48550/arXiv.2412.04557](https://doi.org/10.48550/arXiv.2412.04557)
- Lanz, T., & Hubeny, I. 2007, ApJS, 169, 83, doi: [10.1086/511270](https://doi.org/10.1086/511270)
- Lin, X., Fan, X., Cai, Z., et al. 2025, arXiv e-prints, arXiv:2507.10659, doi: [10.48550/arXiv.2507.10659](https://doi.org/10.48550/arXiv.2507.10659)
- Liu, H., Jiang, Y.-F., Quataert, E., Greene, J. E., & Ma, Y. 2025, ApJ, 994, 113, doi: [10.3847/1538-4357/ae0c19](https://doi.org/10.3847/1538-4357/ae0c19)
- Lyu, J., & Rieke, G. H. 2021, ApJ, 912, 126, doi: [10.3847/1538-4357/abee14](https://doi.org/10.3847/1538-4357/abee14)
- Ma, Y., Greene, J. E., Setton, D. J., et al. 2025, ApJ, 981, 191, doi: [10.3847/1538-4357/ada613](https://doi.org/10.3847/1538-4357/ada613)
- Maiolino, R., Risaliti, G., Signorini, M., et al. 2025, MNRAS, 538, 1921, doi: [10.1093/mnras/staf359](https://doi.org/10.1093/mnras/staf359)
- Mallik, S. V. 1997, A&AS, 124, 359, doi: [10.1051/aas:1997199](https://doi.org/10.1051/aas:1997199)
- Mashonkina, L., Korn, A. J., & Przybilla, N. 2007, A&A, 461, 261, doi: [10.1051/0004-6361:20065999](https://doi.org/10.1051/0004-6361:20065999)
- Matthee, J., Naidu, R. P., Brammer, G., et al. 2024, ApJ, 963, 129, doi: [10.3847/1538-4357/ad2345](https://doi.org/10.3847/1538-4357/ad2345)
- McKemmish, L. K., Masseron, T., Hoeijmakers, H. J., et al. 2019, MNRAS, 488, 2836, doi: [10.1093/mnras/stz1818](https://doi.org/10.1093/mnras/stz1818)
- Meléndez, M., Bautista, M. A., & Badnell, N. R. 2007, A&A, 469, 1203, doi: [10.1051/0004-6361:20077262](https://doi.org/10.1051/0004-6361:20077262)
- Merle, T., Thévenin, F., Pichon, B., & Bigot, L. 2011, MNRAS, 418, 863, doi: [10.1111/j.1365-2966.2011.19540.x](https://doi.org/10.1111/j.1365-2966.2011.19540.x)
- Mihalas, D. 1978, Stellar atmospheres (San Francisco: W. H. Freeman)
- Murray, N., & Chiang, J. 1997, ApJ, 474, 91, doi: [10.1086/303443](https://doi.org/10.1086/303443)
- Naidu, R. P., Matthee, J., Katz, H., et al. 2025, arXiv e-prints, arXiv:2503.16596, doi: [10.48550/arXiv.2503.16596](https://doi.org/10.48550/arXiv.2503.16596)
- Nandal, D., & Loeb, A. 2026, ApJ, 998, 124, doi: [10.3847/1538-4357/ae32f3](https://doi.org/10.3847/1538-4357/ae32f3)
- Osorio, Y., Allende Prieto, C., Hubeny, I., Mészáros, S., & Shetrone, M. 2020, A&A, 637, A80, doi: [10.1051/0004-6361/201937054](https://doi.org/10.1051/0004-6361/201937054)
- Planck Collaboration, Ade, P. A. R., Aghanim, N., et al. 2016, A&A, 594, A13, doi: [10.1051/0004-6361/201525830](https://doi.org/10.1051/0004-6361/201525830)
- Polyansky, O. L., Kyuberis, A. A., Zobov, N. F., et al. 2018, MNRAS, 480, 2597, doi: [10.1093/mnras/sty1877](https://doi.org/10.1093/mnras/sty1877)
- Rinaldi, P., Bonaventura, N., Rieke, G. H., et al. 2024, arXiv e-prints, arXiv:2411.14383, doi: [10.48550/arXiv.2411.14383](https://doi.org/10.48550/arXiv.2411.14383)
- Rusakov, V., Watson, D., Nikopoulos, G. P., et al. 2026, Nature, 649, 574, doi: [10.1038/s41586-025-09900-4](https://doi.org/10.1038/s41586-025-09900-4)
- Sacchi, A., & Bogdan, A. 2025, arXiv e-prints, arXiv:2505.09669, doi: [10.48550/arXiv.2505.09669](https://doi.org/10.48550/arXiv.2505.09669)
- Santarelli, A. D., Farag, E., Bellinger, E. P., et al. 2025, arXiv e-prints, arXiv:2510.17952, doi: [10.48550/arXiv.2510.17952](https://doi.org/10.48550/arXiv.2510.17952)
- Schuster, A. 1905, ApJ, 21, 1, doi: [10.1086/141186](https://doi.org/10.1086/141186)
- Setton, D. J., Greene, J. E., de Graaff, A., et al. 2024, arXiv e-prints, arXiv:2411.03424, doi: [10.48550/arXiv.2411.03424](https://doi.org/10.48550/arXiv.2411.03424)
- Setton, D. J., Greene, J. E., Spilker, J. S., et al. 2025, ApJL, 991, L10, doi: [10.3847/2041-8213/ade78b](https://doi.org/10.3847/2041-8213/ade78b)
- Sneppen, A., Watson, D., Matthews, J. H., et al. 2026, arXiv e-prints, arXiv:2601.18864, <https://arxiv.org/abs/2601.18864>
- Sun, W. Q., Naidu, R. P., Matthee, J., et al. 2026, arXiv e-prints, arXiv:2601.20929, <https://arxiv.org/abs/2601.20929>
- Thompson, T. A., Quataert, E., & Murray, N. 2005, ApJ, 630, 167, doi: [10.1086/431923](https://doi.org/10.1086/431923)
- Torralba, A., Matthee, J., Pezzulli, G., et al. 2025, arXiv e-prints, arXiv:2510.00103, doi: [10.48550/arXiv.2510.00103](https://doi.org/10.48550/arXiv.2510.00103)
- Umeda, H., Inayoshi, K., Harikane, Y., & Murase, K. 2025, arXiv e-prints, arXiv:2512.04208, doi: [10.48550/arXiv.2512.04208](https://doi.org/10.48550/arXiv.2512.04208)
- Underhill, A. B. 1949, ApJ, 110, 340, doi: [10.1086/145211](https://doi.org/10.1086/145211)
- Virtanen, P., Gommers, R., Oliphant, T. E., et al. 2020, Nature Methods, 17, 261, doi: [10.1038/s41592-019-0686-2](https://doi.org/10.1038/s41592-019-0686-2)
- Wang, B., de Graaff, A., Davies, R. L., et al. 2025, ApJ, 984, 121, doi: [10.3847/1538-4357/adc1ca](https://doi.org/10.3847/1538-4357/adc1ca)
- Wang, B., Leja, J., Labbe, I., et al. 2026, arXiv e-prints, arXiv:2602.06024, <https://arxiv.org/abs/2602.06024>
- Williams, C. C., Alberts, S., Ji, Z., et al. 2024, ApJ, 968, 34, doi: [10.3847/1538-4357/ad3f17](https://doi.org/10.3847/1538-4357/ad3f17)
- Xiao, M., Oesch, P. A., Bing, L., et al. 2025, arXiv e-prints, arXiv:2503.01945, doi: [10.48550/arXiv.2503.01945](https://doi.org/10.48550/arXiv.2503.01945)

Yue, M., Eilers, A.-C., Ananna, T. T., et al. 2024, ApJL, 974, L26, doi: [10.3847/2041-8213/ad7eba](https://doi.org/10.3847/2041-8213/ad7eba)
Zhang, C., Wu, Q., Fan, X., et al. 2025, arXiv e-prints, arXiv:2505.12719, doi: [10.48550/arXiv.2505.12719](https://doi.org/10.48550/arXiv.2505.12719)
Zhang, Z., Jiang, L., Liu, W., & Ho, L. C. 2025a, ApJ, 985, 119, doi: [10.3847/1538-4357/adcb3e](https://doi.org/10.3847/1538-4357/adcb3e)

Zhang, Z., Li, M., Oguri, M., et al. 2025b, arXiv e-prints, arXiv:2512.05180, doi: [10.48550/arXiv.2512.05180](https://doi.org/10.48550/arXiv.2512.05180)
Zwick, L., Tiede, C., & Mayer, L. 2025, arXiv e-prints, arXiv:2507.22014, doi: [10.48550/arXiv.2507.22014](https://doi.org/10.48550/arXiv.2507.22014)